

## Improved estimation of cotton (*Gossypium hirsutum* L.) LAI from multispectral data using UAV point cloud data

Lechun Zhang<sup>a</sup>, Binshu Sun<sup>a</sup>, Denan Zhao<sup>a</sup>, Changfeng Shan<sup>a</sup>, Baoju Wang<sup>a</sup>, Guobin Wang<sup>a</sup>, Cancan Song<sup>a</sup>, Pengchao Chen<sup>b,c,\*</sup>, Yubin Lan<sup>a,b,c,d,\*\*</sup>

<sup>a</sup> School of Agricultural Engineering and Food Science, Shandong University of Technology, Zibo, Shandong 255049, China

<sup>b</sup> National Center for International Collaboration Research on Precision Agricultural Aviation Pesticides Spraying Technology (NPAAC), South China Agricultural University, Guangzhou 510642, China

<sup>c</sup> College of Electronic Engineering/College of Artificial Intelligence, South China Agricultural University, Guangzhou 510642, China

<sup>d</sup> National Key Laboratory of Green Pesticide, Guangzhou, Guangdong 5510630, China



### ARTICLE INFO

#### Keywords:

Unmanned aerial vehicle  
Remote sensing  
Data fusion  
Deep learning  
Phenotyping

### ABSTRACT

Real-time monitoring of leaf area index (LAI) in cotton (*Gossypium hirsutum* L.) plays a vital role in guiding field fertilization, water management, growth observation and yield prediction. The use of unmanned aerial vehicles (UAVs) equipped with diverse sensors enables flexible and rapid LAI measurement across extensive areas. This study evaluates the efficacy of UAV-mounted LiDAR and high-resolution camera-derived point cloud data in LAI prediction. We assessed the integration of canopy spectral-textural characteristics from multispectral data with structural features from point cloud data for LAI forecasting. Furthermore, we compared various machine learning and deep learning models, selected the optimal one, and applied the SHAP (Shapley Additive Explanations) method to identify key features and their influence patterns in this model. The findings are distilled into four key points: (1) The performance of canopy structure metrics based on the two sensors varied across fertility periods due to differences in canopy closure; (2) The DNN-based (Deep Neural Network) LAI prediction model excelled with a single-period dataset, achieving an  $R^2$  of 0.81 and an RMSE% of 11.36 %. Similarly, in full-period multimodal data fusion, it demonstrated superior performance, evidenced by an  $R^2$  of 0.84 and an RMSE% of 9.94 %. (3) Compared to the unimodal data model, the multimodal data model yielded superior results and exhibited greater robustness. (4) In the DNN-based LAI prediction model utilizing multimodal data, texture features contributed most significantly. The results suggest that the DNN model, when employing multimodal data fusion, offers not only relatively precise and robust estimates of crop LAI but also contributes valuable insights for crop phenotyping and enhanced field management. This approach subsequently improves spatial prediction accuracy and the quality of decision-making in crop production.

### 1. Introduction

Leaf Area Index (LAI), representing half the total leaf surface area per land area unit, is crucial for characterizing plant growth, as it's intimately linked with vegetation's physiological and biochemical processes (Alton, 2016; Jonckheere et al., 2004). LAI influences multiple aspects of plant growth, including photosynthesis efficiency, water usage, stomatal conductance, and stress tolerance (Asner et al., 1998; Duursma et al., 2016). Additionally, it is also a key factor influencing

vegetation productivity and ecosystem carbon accumulation (Gitelson et al., 2014; Simonich and Hites, 1994). As cotton is a significant economic crop globally, real-time LAI monitoring is essential for guiding field fertilization, water management, growth monitoring, and yield prediction (Chen et al., 2022; Meng et al., 2019). Consequently, precise and timely large-scale prediction of cotton (*Gossypium hirsutum* L.) LAI is vital for enhancing cotton yield and quality (Xu et al., 2021).

In contemporary agricultural practices, LAI is gauged using both direct and indirect field measurement methods (Gower et al., 1999).

\* Corresponding author at: National Center for International Collaboration Research on Precision Agricultural Aviation Pesticides Spraying Technology (NPAAC), South China Agricultural University, Guangzhou 510642, China.

\*\* Corresponding author at: School of Agricultural Engineering and Food Science, Shandong University of Technology, Zibo, Shandong 255049, China.

E-mail addresses: [zhanglechun0710@gmail.com](mailto:zhanglechun0710@gmail.com) (L. Zhang), [pengchao.chen@scau.edu.cn](mailto:pengchao.chen@scau.edu.cn) (P. Chen), [yuan@sdut.edu.cn](mailto:yuan@sdut.edu.cn) (Y. Lan).

Direct measurement involves destructive sampling, rendering it unsuitable for prolonged monitoring (Fang et al., 2019). Indirect measurement, utilizing handheld canopy analyzers like Li-COR LAI-2200 and Sunscan, is labor-intensive and time-consuming (Bréda, 2003; Ryu et al., 2010). Both methods face challenges in large-scale application due to data acquisition limitations. Remote sensing technology facilitates rapid LAI measurement over extensive areas (Camacho et al., 2013; Colomina and Molina, 2014; Ganguly et al., 2008). Unmanned Aerial Vehicles (UAVs) with various image sensors offer higher resolution than satellite images, compensating for satellite remote sensing's inflexibility. UAV remote sensing utilizes two primary sensor types: Active Sensors and Passive Sensors (Toth and Józków, 2016).

Estimation of LAI using UAV-mounted passive sensor data is primarily categorized into: 1) constructing LAI prediction models through statistical regression, utilizing ground-based data and features from remote imagery (Kimura et al., 2004; Viña et al., 2011); and 2) employing radiative transfer models (RTMs) based on canopy biophysical variables, geometric profiles, and reflectance. These methods often face challenges in predicting LAI in dense canopies, as passive sensors have difficulty capturing diverse spatial patterns and heterogeneity (Koetz et al., 2005; Morsdorf et al., 2009). Additionally, LAI predictions from these methods are compromised by saturation issues in dense canopies, due to the limited capability of passive sensors in representing the complex spatial heterogeneity of vegetation (Gitelson et al., 2003; Lüdeke et al., 1991). Integrating three-dimensional plant structural information can more precisely quantify plant growth and capture functional variations of plants across diverse spatial and temporal scales (Dechant et al., 2020; Zhao et al., 2018). Therefore, in order to further improve the prediction accuracy of passive remote sensing sensors LAI can incorporate high-precision 3D plant structure information.

Currently, two primary methods exist for acquiring 3D plant structure information via UAV-mounted sensors: 1) LiDAR on UAVs, which captures structural details of the ground and canopy by emitting lasers to create a 3D dense point cloud (Houldcroft et al., 2005; Liu et al., 2020; Omasa et al., 2007); 2) High-resolution cameras on UAVs, which gather overlapping images. These images are processed with digital photogrammetry and the Structure from Motion (SfM) algorithm to match features and construct 3D dense point clouds (Dandois and Ellis, 2013; Nurminen et al., 2013; Yang et al., 2021a). Both methods can capture 3D plant structural information to varying extents. However, there have been limited studies comparing their effectiveness in predicting LAI under identical flight conditions.

Prior research has utilized canopy height and complexity metrics, including  $H_{max}$  (maximum canopy height),  $H_{mean}$  (mean canopy height),  $H_{std}$  (standard deviation of canopy height), and  $H_{cr}$  (canopy relief height ratio), derived from point clouds, to estimate biophysical variables like LAI and biomass (Li et al., 2015; Næsset and Bjercknes, 2001; Parker and Russ, 2004; Solberg et al., 2009). Additionally, both canopy spectral and texture features, extracted from UAV-borne passive sensors like multispectral and hyperspectral cameras, have proven effective in estimating parameters including crop LAI, leaf chlorophyll content, and yield (Liu et al., 2023; Tahir et al., 2020; Xu et al., 2021; Yang et al., 2021b). Earlier studies indicate that integrating canopy spectral, texture, and structural features from various sensors enhances the accuracy of plant trait estimation. However, limited research exists on merging canopy-related metrics from point clouds with passive sensor imagery features for LAI prediction.

Recently, the advancement of computer technology has enabled the application of machine learning-based regression methods, including Partial Least Squares Regression (PLSR), Random Forest Regression (RFR), Support Vector Machine (SVM), and Gradient-Boosting Decision Tree (GBDT), in predicting LAI for diverse plant species (Durbha et al., 2007; Houborg and McCabe, 2018; Lan et al., 2017; Shao et al., 2023; Zhang et al., 2024). Deep learning, a subset of machine learning, enhances prediction accuracy for large, complex datasets. Deep Neural Networks (DNNs), a deep learning technique, have demonstrated

effectiveness in various agricultural remote sensing applications, including regression and classification tasks (Ball et al., 2017; Cai et al., 2018; Liu et al., 2021). However, there are limited studies employing deep learning for crop LAI prediction, and none have yet explored predicting crop LAI by integrating canopy-related metrics from point clouds with features from passive sensor imagery within a deep neural network framework.

This study aims to: (1) compare the efficacy of UAV-mounted LiDAR and high-resolution RGB camera-derived point cloud data in LAI prediction; (2) evaluate the effectiveness of integrating canopy spectral, textural, and point cloud structural features from multispectral data for LAI estimation; and (3) assess various machine learning models to identify the most effective model, determine its most influential features, and analyze the pattern of their impact.

## 2. Materials

### 2.1. Experimental site and design

The study was carried out in Bincheng District, Binzhou City, Shandong Province, China, characterized by a temperate monsoon climate (Fig. 1). The cotton variety used is LU37, the row spacing is 0.75 m, and the plant spacing is 0.15 m. The size of each LAI ground data sampling area is 3 m × 3 m, and 12 groups of sampling areas are set for each nitrogen treatment, resulting in a total of 48 LAI ground data sampling areas. The distribution of the LAI ground data sampling areas is shown in Fig. 1. This region receives an average annual precipitation of 562.5 mm, experiences an average evapotranspiration of 1758.9 mm, and enjoys 2526.9 hours of sunshine annually. The experiment involved four nitrogen fertilizer treatments: N0 (0 kg/hm<sup>2</sup>), N1 (120 kg/hm<sup>2</sup>), N2 (240 kg/hm<sup>2</sup>), and N3 (360 kg/hm<sup>2</sup>). Ten ground control points (GCPs) were established in the experimental field. Precise latitude and longitude data were recorded to ensure geographic alignment, with four GCPs allocated around the field for each nitrogen fertilizer level.

### 2.2. Data acquisition and preprocessing

#### 2.2.1. LAI data acquisition

This study involved collecting LAI data for cotton during five critical growth periods using the ground-based SunScan plant canopy analyzer (Delta-TI Devices, Cambridge, UK). The SunScan's 1 m-long probe is equipped with 64 photosensors to measure transmittance. These sensors, together with a beam fraction sensor (BFS), calculate the LAI based on the Beer-Lambert law, with results displayed on a personal digital assistant (PDA). LAI values were recorded at 45° intervals in four directions around each cotton plant. Measurements were repeated thrice per direction, and the average values were retained. LAI ground data were collected during five key growth stages of cotton, The Squaring Stage (June 30, 2023), The Flowering and boll Stage (July 17, 2023), The Cracking Stage (August 23, 2023), The Boll opening stage (September 14, 2023), The stop-growing stage (September 30, 2023). Each LAI ground data sampling area was sampled twice during each sampling period. A total of 480 sets of LAI ground measurement data were collected during the entire growth period. In order to verify the accuracy of the UAV sensor in extracting structure-related features, the CH of cotton at the center of the LAI ground data sampling area (48) and the four vertices (16) of each nitrogen treatment area (16) were measured from the ground in each period. A total of 320 sets of LAI ground measurement data were collected during this period. Statistical results of the field measurements are presented in Table 1. The distribution of LAI in each period is shown in Fig. 2.

#### 2.2.2. UAVs data acquisition

Remote sensing images from the UAV and field measurements of LAI were conducted simultaneously on the same day, between 10:00 and 14:00. High-resolution RGB images (Fig. 3b) were captured using a DJI

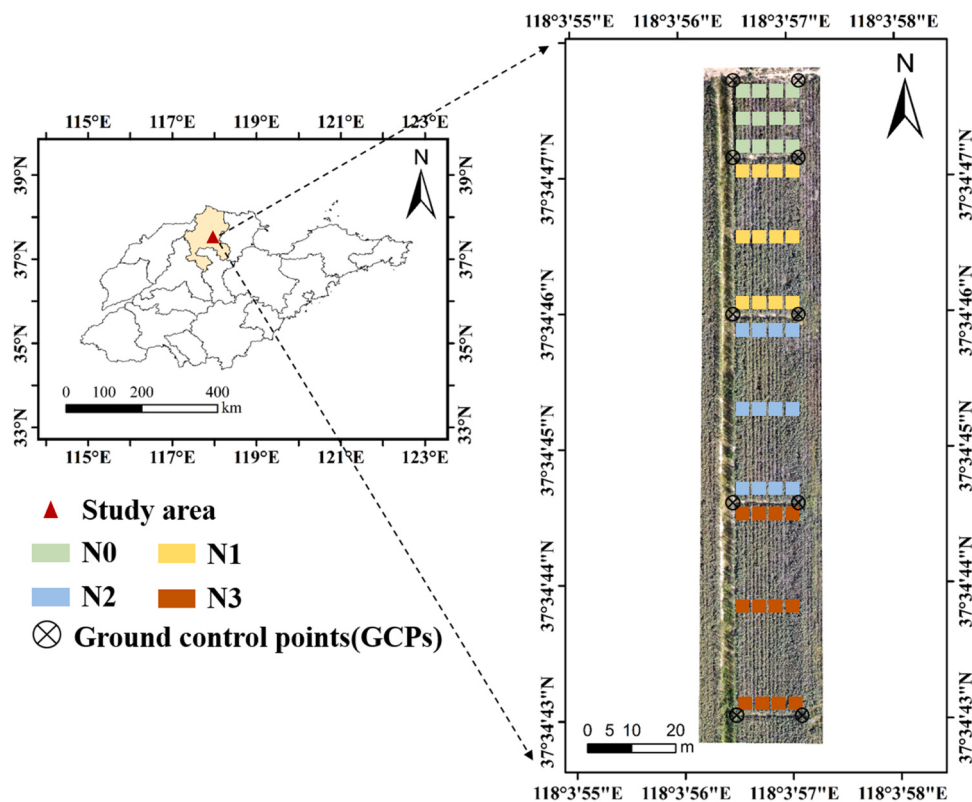


**Fig. 1.** Experimental area Note: N0, N1, N2, N3 represent different nitrogen fertilizer treatments, and the squares represent the ground sampling area of LAI.

**Table 1**

Descriptive statistics of LAI and CH at different growth stages of cotton.

| Parameters | Date               | NO. of samples | Mean | Max  | Min  | SD   | CV(%)   |
|------------|--------------------|----------------|------|------|------|------|---------|
| LAI        | June 30, 2023      | 96             | 0.97 | 3.44 | 0.12 | 0.59 | 60.63 % |
|            | July 17, 2023      | 96             | 3.35 | 5.53 | 0.43 | 1.37 | 40.86 % |
|            | August 23, 2023    | 96             | 4.18 | 6.47 | 0.89 | 1.14 | 27.27 % |
|            | September 14, 2023 | 96             | 3.45 | 5.46 | 0.67 | 0.98 | 28.37 % |
|            | September 30, 2023 | 96             | 2.34 | 3.93 | 0.57 | 0.78 | 33.32 % |
| CH ( m )   | June 30, 2023      | 64             | 0.64 | 0.86 | 0.21 | 0.12 | 18.69 % |
|            | July 17, 2023      | 64             | 0.96 | 1.29 | 0.44 | 0.15 | 15.58 % |
|            | August 23, 2023    | 64             | 1.21 | 1.55 | 0.61 | 0.17 | 14.02 % |
|            | September 14, 2023 | 64             | 1.32 | 1.62 | 1.03 | 0.11 | 8.30 %  |
|            | September 30, 2023 | 64             | 1.31 | 1.60 | 1.06 | 0.11 | 8.36 %  |

Note : SD: standard deviation ; CV: coefficient of variation.

Matrice 300 RTK (M300) UAV equipped with a Zenmuse P1 sensor, with an 80 % heading overlap, 80 % lateral overlap, and a flight speed of 1 m/s. LiDAR data (Fig. 3a) were collected using the same DJI Matrice 300 RTK (M300) UAV, equipped with a Zenmuse L1 sensor. The point cloud overlap was set at 10 %, the sampling frequency at 240 kHz, and the flight speed at 1 m/s, utilizing a double-pulse scan. Multi-spectral images (Fig. 3c) were obtained using a DJI Phantom 4 Multi-spectral (P4M) UAV, with 80 % heading and lateral overlaps and a flight speed of 1 m/s. The professional UAVs provided by DJI have a centimeter-level RTK positioning system. When using RTK positioning, the position accuracy in the horizontal direction is: 1 cm+1 ppm (1 ppm means that the error increases by 1 mm for every 1 km the aircraft moves), the position accuracy in the vertical direction is 1.5 cm + 1 ppm. A standard reflectance panel was photographed before each acquisition for radiometric correction (Fig. 3d). The multispectral sensor's parameters are detailed in Table 2. All three sensors were operated at a flight altitude of

30 m to facilitate the comparative analysis of SfM photogrammetry and LiDAR point cloud performance under uniform flight conditions.

### 2.2.3. MS Imagery preprocessing

Image stitching for multispectral and RGB images was conducted using Pix4Dmapper (Pix4D SA, Lausanne, Switzerland). During image stitching, the images were geo-aligned using GCPs to enhance the accuracy of the resulting orthophotos. Radiometric correction, using images of standard reflectance panels, was also performed for multispectral imagery during the stitching process. A Support Vector Machine (SVM) classifier in ArcGIS 10.6 (ESRI, Redlands, CA, USA) was utilized to distinguish between vegetation and soil in the UAV images. From the classification results, a binary mask map was created, enabling the removal of soil pixels for subsequent analysis. The classifier's performance was evaluated using overall accuracy and Kappa coefficient. The overall accuracies for the five periods varied between 92.9 % and

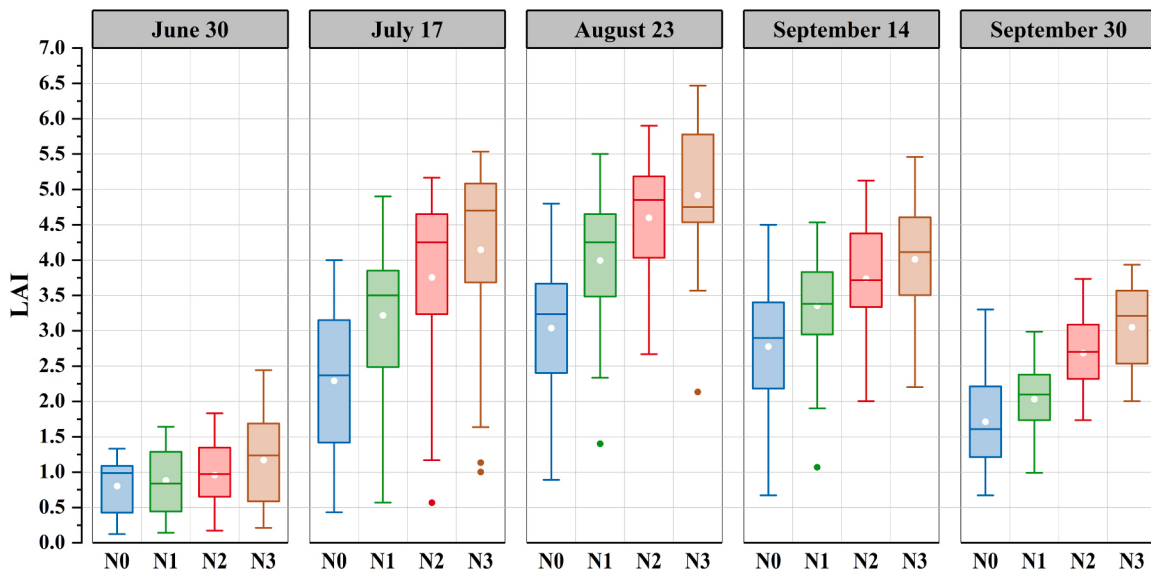


**Fig. 2.** The distribution of LAI in each period. Note: N0, N1, N2, N3 represent different nitrogen fertilizer treatments.



**Fig. 3.** Sensors carried by the UAV ( a ) DJI M300 with Zenmuse L1, ( b ) DJI M300 with Zenmuse P1, ( c ) DJI P4M with multispectral sensor, and ( d ) radiative correction of the multispectral sensor. Note: The red box in ( a ) is the Zenmuse L1 sensor, the yellow box in ( b ) is the Zenmuse P1 sensor, the green box in ( c ) is the multispectral sensor of the DJI P4M, and the blue box in ( d ) is the image acquisition of the standard reflectance panel.

96.4 %, with Kappa coefficients from 0.927 to 0.967. High-density point clouds in LAS (Point Cloud Data Storage File Extension) format were produced from the high-resolution RGB images using the SfM technique in Pix4Dmapper. Point cloud data, inertial guide records, and trajectory information from LiDAR were processed using DJI Terra (SZ DJI Technology Co., Ltd., Shenzhen, China). The LAS file was produced following image stitching and point cloud coloring operations.

### 3. Method

#### 3.1. Canopy feature extraction

##### 3.1.1. Canopy spectral features

In this study, 28 vegetation indices (VIs) commonly used for estimating LAI were constructed using UAV multispectral imagery, and

**Table 2**  
Basic parameters of the MS sensor.

| Band Name          | Wavelength | Bandwidth | Image Resolution |
|--------------------|------------|-----------|------------------|
| Red(R)             | 450 nm     | ±16 nm    | 1600×1300        |
| Green(G)           | 560 nm     | ±16 nm    |                  |
| Blue(B)            | 650 nm     | ±16 nm    |                  |
| Red edge(RE)       | 730 nm     | ±16 nm    |                  |
| Near infrared(NIR) | 840 nm     | ±26 nm    |                  |

ENVI5.3 (L3Harris Technologies, Melbourne, FL, USA) software was used to construct the vector files of different plots and complete the data statistics of the different partitions. The VIs used in this study are shown in Table 3.

### 3.1.2. Canopy texture features

In this study, texture features are extracted from five raw bands of multispectral images as canopy texture features. The gray-level co-occurrence matrix (GLCM) algorithm was used in this study to extract the texture features (Haralick et al., 1973). A 7 × 7 window was set up in ENVI 5.3 software to extract eight canopy texture features, including mean (MEA), variance (VAR), homogeneity (HOM), contrast (CON),

**Table 3**  
Vegetation indices formula for UAV multispectral images.

| Spectral Indices                                     | Definition  | References                    |
|--|---|-------------------------------|
| Ratio Between NIR and Green Bands                    | $VI_{(nir/green)} = \frac{R_{nir}}{R_{green}}$  | (Gitelson and Merzlyak, 1997) |
| Ratio Between NIR and Red Bands                      | $VI_{(nir/red)} = \frac{R_{nir}}{R_{red}}$  | (Ramoelo et al., 2012)        |
| Ratio Between NIR and Red Edge Bands                 | $VI_{(nir/rededge)} = \frac{R_{nir}}{R_{rededge}}$  | (Ramoelo et al., 2012)        |
| Non Linear Index                                     | $NLI = \frac{R_{nir}^2 - R_{red}}{R_{nir}^2 + R_{red}}$   | (Goel and Qin, 1994)          |
| MERIS Terrestrial Chlorophyll Index                  | $MTCI = \frac{R_{nir} - R_{rededge}}{R_{rededge} - R_{red}}$  | (Dash and Curran, 2004)       |
| Transformed Soil Adjusted Vegetation Index           | $TSAVI = \frac{a \times (R_{nir} - a \times R_{red} - b)}{a \times R_{nir} + a \times R_{red} - a \times b}$ ( $a = 10.489, b = 6.604$ )  | (Baret and Guyot, 1991)       |
| Normalized Difference Vegetation Index               | $NDVI = \frac{R_{nir} - R_{red}}{R_{nir} + R_{red}}$  | (Myndeni and Williams, 1994)  |
| Difference Vegetation Index                          | $DVI = R_{nir} - R_{red}$   | (Tucker, 1979)                |
| Optimized SAVI                                       | $OSAVI = (1 + 0.16) \times \frac{R_{nir} - R_{red}}{R_{nir} + R_{red} + 0.16}$  | (Rondeaux et al., 1996)       |
| SAVI   | $SAVI = (1 + 0.5) \times \frac{R_{nir} - R_{red}}{R_{nir} + R_{red} + 0.5}$   | (Huete, 1988)                 |
| Green Normalized Difference Vegetation               | $GNDVI = \frac{R_{nir} - R_{green}}{R_{nir} + R_{green}}$   | (Gitelson et al., 1996)       |
| Atmospherically<br>resistant vegetation index        | $ARVI = \frac{R_{nir} - (2 \times R_{red} - R_{blue})}{R_{nir} + (2 \times R_{red} - R_{blue})}$  | (Kaufman and Tanre, 1992)     |
| renormalized difference vegetation index             | $RDVI = \frac{R_{nir} - R_{red}}{\sqrt{R_{nir} + R_{red}}}$   | (Roujean and Breon, 1995)     |
| triangular vegetation index                          | $TVI = 60 \times (R_{nir} - R_{red}) - 100 \times (R_{red} - R_{green})$  | (Broge and Leblanc, 2001)     |
| Modified Triangular Vegetation Index 2               | $MTVI2 = \frac{1.5 \times [1.2 \times (R_{nir} - R_{green}) - 2.5 \times (R_{red} - R_{green})]}{\sqrt{(2 \times R_{nir} + 1)^2 - (6 \times R_{nir} - 5 \times \sqrt{R_{nir}}) - 0.5}}$ | (Haboudane et al., 2004)      |
| Enhanced Vegetation Index                            | $EVI = \frac{2.5 \times (R_{nir} - R_{red})}{a \times R_{nir} + a \times R_{red} - a \times b}$   | (Huete et al., 2002)          |
| Normalized Difference Red Edge Index                 | $NDRE = \frac{R_{nir} - R_{rededge}}{R_{nir} + R_{rededge}}$  | (Gitelson and Merzlyak, 1994) |
| Modified Soil Adjusted Vegetation Index              | $MSAVI = (1 + L) \left( \frac{R_{nir} - R_{red}}{R_{nir} + R_{red} + L} \right)$ ( $L = 0.1$ )  | (Qi et al., 1994)             |
| Modified SAVI 2                                      | $MSAVI2 = R_{nir} + 0.5 - \frac{\sqrt{(2 \times R_{nir} + 1)^2 - 8 \times (R_{nir} - R_{red})}}{2}$   | (Qi et al., 1994)             |
| Normalized Difference Index                          | $NDI = \frac{R_{nir} - R_{rededge}}{R_{nir} + R_{red}}$   | (Datt, 1999)                  |
| Red-Edge Chlorophyll Index 1                         | $CI1 = \frac{R_{nir}}{R_{rededge}} - 1$   | (Li et al., 2012)             |
| Red-Edge Chlorophyll Index 2                         | $CI2 = \frac{R_{rededge}}{R_{green}} - 1$   | (Gitelson and Merzlyak, 1996) |
| Modified Simple Ratio                                | $MSR = \frac{\frac{R_{nir}}{R_{red}} - 1}{\sqrt{\frac{R_{nir}}{R_{red}}} + 1}$  | (Chen, 1996)                  |
| Modified Chlorophyll Absorption Reflectance Index    | $MCARI = (R_{rededge} - R_{red} - 0.2 \times (R_{rededge} - R_{green})) \times \left( \frac{R_{rededge}}{R_{red}} \right)$  | (Daughtry et al., 2000)       |
| Modified Chlorophyll Absorption Reflectance Index 2  | $MCARI2 = 1.5 \times \frac{2.5 \times (R_{nir} - R_{rededge}) - 1.3 \times (R_{nir} - R_{green})}{2 \times (R_{nir} + 1)^2 - (6 \times R_{nir} - 5 \times (R_{red})^2) - 0.5}$          | (Haboudane et al., 2004)      |
| Transformed Chlorophyll Absorption Reflectance Index | $TCARI = 3 \times ((R_{rededge} - R_{red}) - 0.2 \times (R_{rededge} - R_{green})) \times \left( \frac{R_{rededge}}{R_{red}} \right)$   | (Haboudane et al., 2002)      |
| Simplified Canopy Chlorophyll Content Index          | $SCCCI = \frac{NDRE}{NDVI}$   | (Raper and Varco, 2015)       |
| kernel NDVI  | $kNDVI = \tanh \left( \frac{(R_{nir} - R_{red})^2}{2\sigma} \right)$ ( $\sigma = 0.5(R_{nir} + R_{red})$ )  | (Camps-Valls et al., 2021)    |

dissimilarity (DIS), entropy (ENT), second moment (SE) and correlation (COR).

### 3.1.3. Point cloud-based metrics extraction

Noise filtering for LiDAR and RGB photogrammetry-derived point cloud data was conducted using LiDAR360 software (Beijing Green Valley Technology Co., Ltd., Beijing, China), aimed at eliminating high and low gross errors. Ground points in LiDAR-based point cloud data were classified using the Improved Progressive TIN Densification (IPTD) algorithm (Zhao et al., 2016). This algorithm grids the point cloud data and selects the lowest point in each grid as the starting seed point. An initial sparse triangular mesh structure is constructed from these seed points, followed by iterative TIN densification. During this process, each point's maximum distance ( $d$ ) and angles ( $\alpha_1, \alpha_2, \alpha_3$ ) from the triangle's vertices are computed, based on their horizontal projection onto the triangle, as shown in Fig. 4. Points meeting preset thresholds for distance and angle are classified as ground points and added to the triangular mesh. This classification iterates until all ground points are identified. Ground and non-ground points were then rasterized to generate the Digital Elevation Model (DEM) and Digital Surface Model (DSM), from which the vegetation canopy height model (CHM) was derived by calculating the difference between the DSM and DEM.

For the RGB photogrammetric point cloud, high-resolution images of bare earth were captured, and a DEM was created on May 15, 2023, before plant emergence. This was due to the limited penetration ability of passive sensors, which hinders accurate terrain elevation data generation. Subsequently, high-resolution RGB images from each period were employed to independently construct a DSM. The pixel differences between the DSM and DEM were then calculated for each period to develop the CHM.

Canopy structure indicators from LiDAR and RGB photogrammetry were independently extracted, as detailed in Table 4. This table presents 27 sets of indicators, including fifteen sets of canopy height percentiles, providing insights into both the distribution and the vertical complexity and heterogeneity of canopy composition. Utilizing the unique characteristics of both sensors, Canopy Cover (CC) was derived through two distinct methods (Ma et al., 2017). According to whether the point cloud data has echo information, two methods of calculating CC are used. If the point cloud data has echo information, for a certain statistical unit, the value of CC is the number of vegetation points of the first echo and the number of first echo points. Ratio; if the point cloud data does not have echo information, for a certain statistical unit, the canopy density can be calculated as the ratio of the number of vegetation points to the total number of points. The CH obtained from the RGB photogrammetric point cloud was then compared with manual ground-based CH

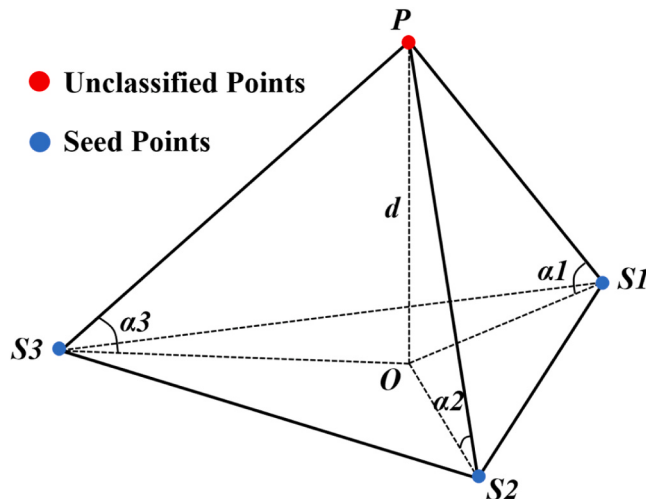


Fig. 4. Schematic of the iteration angle  $\alpha$  and the iteration distance  $d$ .

Table 4

Canopy structure-based metrics.

| Canopy structure-based metrics               | Definition   |
|--|--|
| Maximum canopy height                        | $H_{\max} = \text{MAX}(H_i)$   |
| Minimum canopy height                        | $H_{\min} = \text{MIN}(H_i)$   |
| Mean canopy height                           | $H_{\text{mean}} = \left(\frac{1}{n}\right) \times \sum_{i=1}^n H_i$               |
| The standard deviation of canopy height      | $H_{\text{sd}} = \sqrt{\frac{\sum_{i=1}^n (H_i - H_{\text{mean}})^2}{n-1}}$        |
| Coefficient of variation of canopy height    | $H_{\text{cv}} = \frac{H_{\text{sd}}}{H_{\text{mean}}}$                            |
| Mean Absolute Deviation of canopy height     | $H_{\text{mad}} = \frac{\sum_{i=1}^n  H_i - H_{\text{mean}} }{n}$                  |
| Median of canopy height                      | $H_{\text{med}} = \text{MED}(H_i)$   |
| Percentile of canopy height                  | $H_P = \text{Percentile}(H_i, P)$  |
| The Interquartile Range of canopy height     | $H_{\text{iqr}} = H_{75\%} - H_{25\%}$   |
| Skewness of canopy height                    | $H_{\text{ske}} = \frac{1}{n-1} \sum_{i=1}^n (H_i - H_{\text{mean}})^3 / \sigma^3$ |
| Kurtosis of canopy height                    | $H_{\text{kur}} = \frac{1}{n-1} \sum_{i=1}^n (H_i - H_{\text{mean}})^4 / \sigma^4$ |
| Canopy relief ratio of height                | $H_{\text{cr}} = \frac{H_{\text{mean}} - H_{\min}}{H_{\max} - H_{\min}}$           |
| Canopy Cover derived from LiDAR              | $CC_{\text{LiDAR}} = \frac{n_{\text{vegfirst}}}{n_{\text{first}}}$                 |
| Canopy Cover derived from RGB photogrammetry | $CC_{\text{RGB}} = \frac{n_{\text{veg}}}{n_{\text{total}}}$                        |

Note:  $H_i$ : Height value of the  $i^{th}$  point in a statistical cell.  $n$ : Total number of points in a statistical cell.  $P$ : Height percentile, encompassing 15 percentiles (1 %, 5 %, 10 %, 20 %, 25 %, 30 %, 40 %, 50 %, 60 %, 70 %, 75 %, 80 %, 90 %, 95 %, 99 %).  $\sigma$ : Standard deviation of the height distribution in the point cloud.  $n_{\text{vegfirst}}$ : Number of vegetation points in the first return of the LiDAR.  $n_{\text{first}}$ : Total number of points in the first return of the LiDAR.  $n_{\text{veg}}$ : Number of vegetation points.  $n_{\text{total}}$ : Total number of points.

measurements. Additionally, 320 ground-based CH measurements were employed to assess the accuracy of the CHM, with results displayed in Fig. 5.

### 3.2. LAI prediction model construction and validation

#### 3.2.1. Modeling methods

Multimodal data fusion involves integrating features from diverse sources to enhance information completeness and decision accuracy. In multimodal data fusion, each modality contributes a unique perspective, and their combination yields richer, more comprehensive insights than a single modality alone. Multimodal data fusion occurs at three levels: input level fusion, feature level fusion, and decision level fusion. This study employs input-level feature fusion to predict cotton LAI within a fully-connected feedback DNN framework. The architecture of the input-level feature multimodal DNN developed for this study is depicted in Fig. 6. The DNN comprises one input layer, three hidden layers (each with 10 neurons), and one output layer. The hidden layers include three convolutional layers. The Rectified Linear Unit (ReLU), defined as  $f(z) = \max(0, z)$ , is selected as the activation function. The Adam optimizer is utilized to expedite gradient descent, factoring in the exponential decay averaging of past gradients and automatically adjusting each parameter's learning rate. Mean Square Error (MSE) calculates the model's loss, while L2 regularization distributes the weight values to mitigate overfitting in the DNN, as demonstrated in the following equation:

$$L = \frac{1}{n} \sum_{i=1}^n (y_i - \hat{y}_i)^2 + \lambda \sum_{i=1}^n w_i^2 \quad (1)$$

where  $L$  is the loss function value,  $n$  is the number of samples,  $y_i$  is the  $i^{th}$  sample value,  $\hat{y}_i$  is the predicted value of the  $i^{th}$  sample,  $\lambda$  is the regularization coefficient, and  $\sum_{i=1}^n w_i^2$  is the sum of squares of all the weights

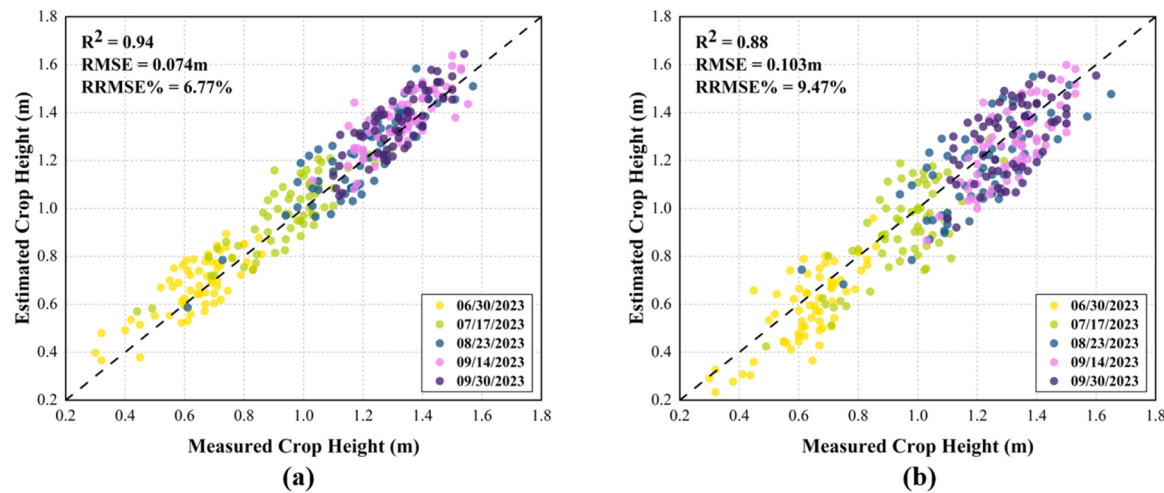


Fig. 5. Relationship between LiDAR and RGB photogrammetry-derived CH and measured CH.

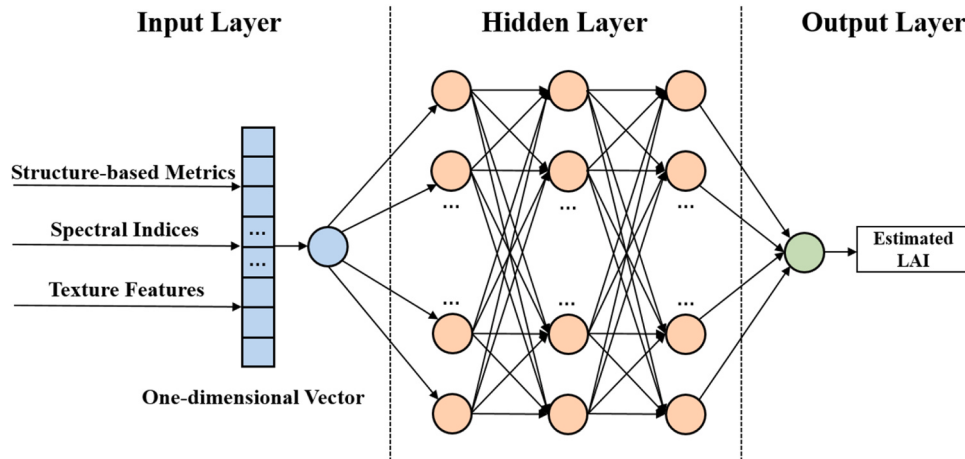


Fig. 6. The network structure schematic of the multimodal DNN model constructed in this study. Note: The circles denote the neural units.

of the model.

Machine learning regression models, including PLSR, SVM, and RFR, are constructed. DNN models are implemented using Python with TensorFlow and Keras libraries, while PLSR, SVM, and RFR utilize Python and Scikit-learn libraries. To ensure a fair and uniform comparison between machine learning and deep learning methods, 70 % of the input features and observed LAI data are randomly selected for model training. The remaining 30 % are used for testing the model's performance and accuracy. The performance of the LAI prediction model is evaluated using the coefficient of determination ( $R^2$ ), root mean square error (RMSE), relative RMSE (RMSE%), and mean absolute error (MAE), calculated as follows:

$$R^2 = \sum_{i=1}^n (\hat{y}_i - \bar{y}) (y_i - \bar{y}) / \sqrt{\sum_{i=1}^n (\hat{y}_i - \bar{y})^2 \sum_{i=1}^n (y_i - \bar{y})^2} \quad (2)$$

$$RMSE = \sqrt{\frac{\sum_{i=1}^n (\hat{y}_i - y_i)^2}{n}} \quad (3)$$

$$RMSE\% = \left( \sqrt{\frac{\sum_{i=1}^n (\hat{y}_i - y_i)^2}{n}} \right) / \bar{y} \quad (4)$$

$$MAE = \sum_{i=1}^n |\hat{y}_i - y_i| / n \quad (5)$$

Where  $n$  denotes the total number of samples;  $\hat{y}_i$  denotes the LAI estimate;  $y_i$  denotes the LAI measurements; and  $\bar{y}$  denotes the mean of the LAI measurements.

### 3.2.2. Model interpretation with the SHAP method

The fundamental concept of SHAP (Shapley Additive Explanations) is based on cooperative game theory, wherein each feature is viewed as a player or contributor. Within this framework, Shapley values are used to fairly allocate the contribution of each feature to the model's predictions. In SHAP, the original input feature  $x$  is transformed into a new, simplified input space, denoted as  $z$ , with the transformed input represented as  $zx = h_x(z)$ . Consequently, the original model  $f(x)$  is approximated using a linear function of binary variables, expressed as follows:

$$f(x) = g(z) = \varphi_0 + \sum_{i=1}^M \varphi_i z_i \quad (6)$$

Where  $M$  is the number of input features,  $z_i=1$  indicates that the original feature  $x_i$  is included in the prediction, whereas  $z_i=0$  signifies that  $x_i$  is excluded,  $\varphi_0 = f(h_x(0))$ , and  $\varphi_i$  is the feature attribution value:

$$\varphi_i = \sum_{S \in F \setminus \{i\}} \frac{|S|!(M - |S| - 1)!}{M!} [f_x(S \cup \{i\}) - f_x(S)] \quad (7)$$

$$f_x(S) = f(h_x^{-1}(z)) = E[f(x)|x_s] \quad (8)$$

Where  $F$  is the set of all features,  $S$  represents all possible subsets of features excluding  $i$ ,  $f_x(S \cup \{i\})$  and  $f_x(S)$  are the model predictions with and without the feature  $i$ ,  $\varphi_i$  represents the unified metric of additive feature attributions, known as the SHAP value.

Given the challenge in accurately computing the conditional expectation  $E[f(x)|x_s]$ , several approximation methods, such as Kernel SHAP, have been developed. Kernel SHAP, a kernel-based approach, is employed for estimating SHAP values. This method, by accounting for all possible feature subsets and assigning corresponding weights, can efficiently approximate the contributions of model predictions. This provides valuable insights into the decision-making process, making it

applicable to various machine learning and deep learning models. In this study, SHAP for model interpretation is implemented using Python and the SHAP package. The study's workflow, from feature extraction to model construction, is depicted in Fig. 7.

#### 4. Results and discussion

##### 4.1. Correlation analysis of canopy structure indicators based on LiDAR and RGB photogrammetry

Correlation analysis was conducted between canopy structure metrics extracted from LiDAR and RGB photogrammetry and LAI. The strength of these correlations was evaluated using the Pearson correlation coefficient. Generally, combining data from multiple periods for correlation analysis is more effective than using single-period data. This approach yields a broader range of values in the dataset, enhancing data

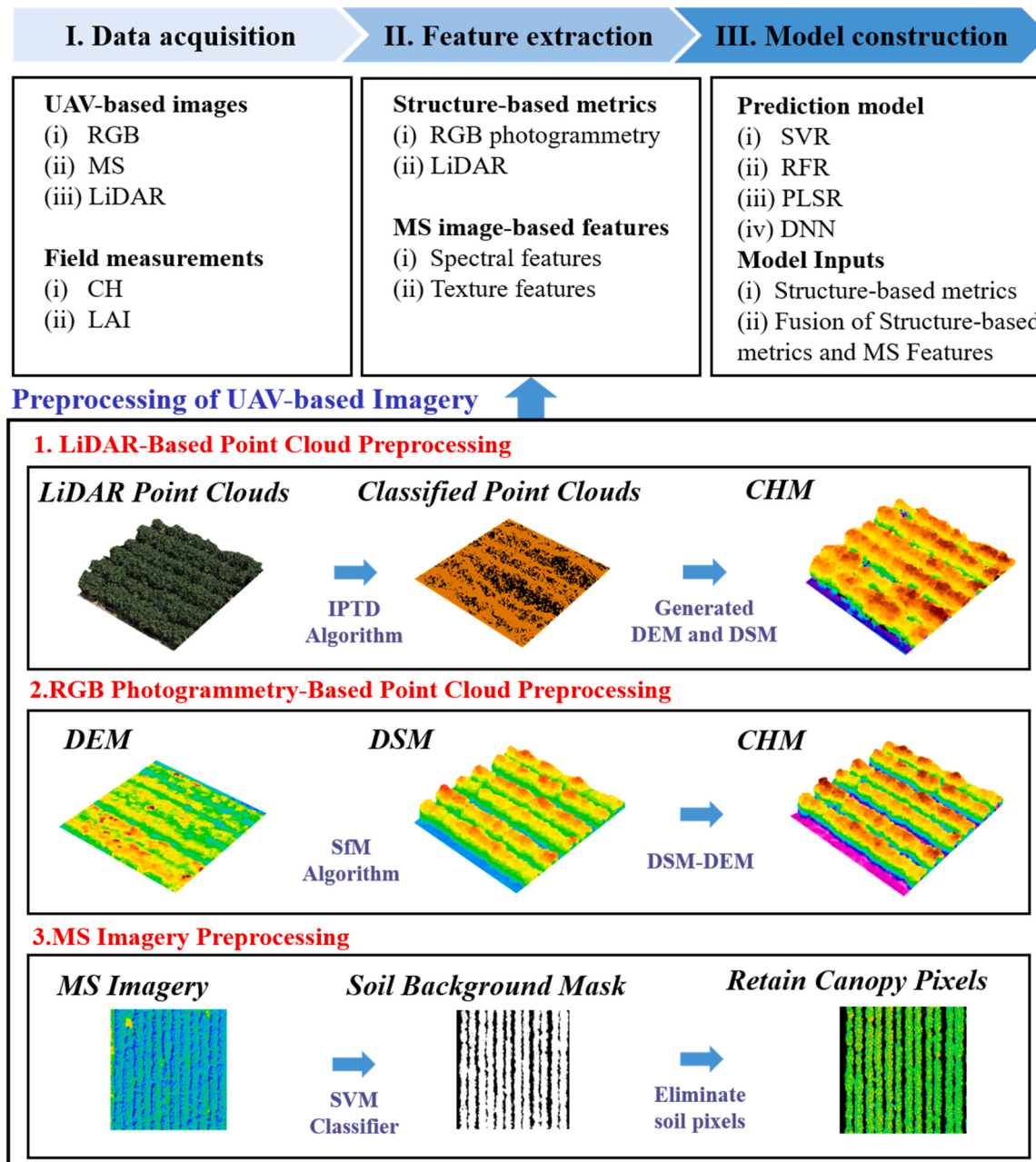


Fig. 7. Workflow diagram.

variability and enabling the capture of more complex or subtle relationships among variables. Considering that cotton growth is a seasonal and dynamic process, data from multiple dates offers a more comprehensive view. Consistency across these data points strengthens correlation signals, rendering the correlations more evident and plausible. The results of this multi-period correlation analysis are presented in Fig. 8.

The study compared the correlation of LiDAR-based canopy structure metrics with LAI against that of RGB photogrammetry-based canopy structure metrics with LAI. According to Fig. 8(a), most LiDAR-based canopy structure metrics, notably  $H_{max}$ ,  $H_{mean}$ , and various canopy height percentiles ( $H_{60}$  to  $H_{99}$ ), exhibited positive correlations with LAI. However, the  $H_{sd}$  and  $H_{cv}$  of canopy height demonstrated only weak correlations with LAI. This suggests that while overall canopy height correlates with LAI, the heterogeneity in canopy height may not significantly influence LAI. Similarly, as depicted in Fig. 8(b), most RGB photogrammetry-based canopy structure metrics, like LiDAR data, exhibited positive correlations with LAI. This indicates consistency across different techniques in assessing the canopy-LAI relationship. Compared to LiDAR-based data, the correlations of  $H_{max}$  and  $H_{mean}$  with LAI were found to be lower. However, the correlation of certain metrics such as the  $H_{cv}$  and  $H_{sd}$  with LAI was more pronounced. This could be attributed to the SfM algorithm of the RGB camera, which constructs a 3D model from multiple 2D images, potentially amplifying local height variability, especially with errors from interpolation and smoothing during reconstruction. This method likely captures increased local variability, thereby exhibiting a stronger correlation with LAI. Additionally, due to the sensitivity of RGB images to lighting conditions, lighting and shading can introduce extra height variance during the SfM algorithm's operation. This variance may correlate more strongly with LAI, as it enhances image textures and edges, leading to greater height differences in the reconstructed canopy model (Volpatto et al., 2021).

It is worth mentioning that the correlation between Percentile of canopy height obtained based on both methods tended to become larger with increasing percentile, and the correlation between LiDAR-based Percentile of canopy height and LAI was higher at lower percentiles, with LiDAR possibly being more accurate due to its high penetration is more reflective of the true height of the bottom of the canopy, whereas the SfM algorithm is less accurate due to viewpoint limitations (Madec et al., 2017; Nie et al., 2016). The accuracy advantage of LiDAR

measurements is also more obvious at the high percentile, where the laser is not only able to penetrate the canopy and reach the structure below the vegetation to obtain complete height information from the top to the bottom of the canopy, but it is also usually unaffected by changes in ambient light, and therefore can capture the vertical structure of the canopy very accurately and precisely (Jin et al., 2021; Luo et al., 2017).

We also conducted correlation analysis on data from individual periods, and the results are presented in Table 5. The overall correlation trend of each canopy structure index resembles that of the multi-period combination results. However, it is worth noting that during the early stage of crop growth (June 30, 2023), the correlation between each point cloud-based canopy structure index and LAI was lower compared to other periods. This may be attributed to the lower height of cotton plants and significant gaps between them at this time, resulting in substantial differences in ground-level LAI values measured from various angles. Consequently, this leads to larger errors in ground-level LAI and, consequently, lower correlations compared to other periods. Most of the peaks in the correlations of the point cloud-based canopy structure indices occurred on August 23, 2023 and September 14, 2023, when the canopy had expanded to its maximum and the LAI measurements stabilized, resulting in stronger correlations. On September 30, 2023, the correlation decreased as many leaves had senesced and fallen off.

#### 4.2. LAI prediction model construction for canopy structure metrics based on LiDAR and RGB photogrammetry

In this study, in order to investigate the ability of canopy structure indicators based on UAV LiDAR and RGB photogrammetry in predicting LAI, a prediction model was constructed using measured data from five periods of cotton and 27 sets of canopy structure indicators based on UAV LiDAR and RGB photogrammetry, respectively. The prediction results of the models are shown in Table 6.

The results indicate that LAI estimation using LiDAR-based canopy structure metrics generally surpasses that using RGB photogrammetry-based metrics, with the exception of the dataset from September 30, 2023. This superiority is attributed to LiDAR's high penetration capability, which enables it to measure the entire canopy structure, from top to bottom, providing comprehensive height information crucial for accurate LAI prediction. And the prediction accuracy reached its highest at September 14, 2023, with the  $R^2$  of each machine learning model for LAI

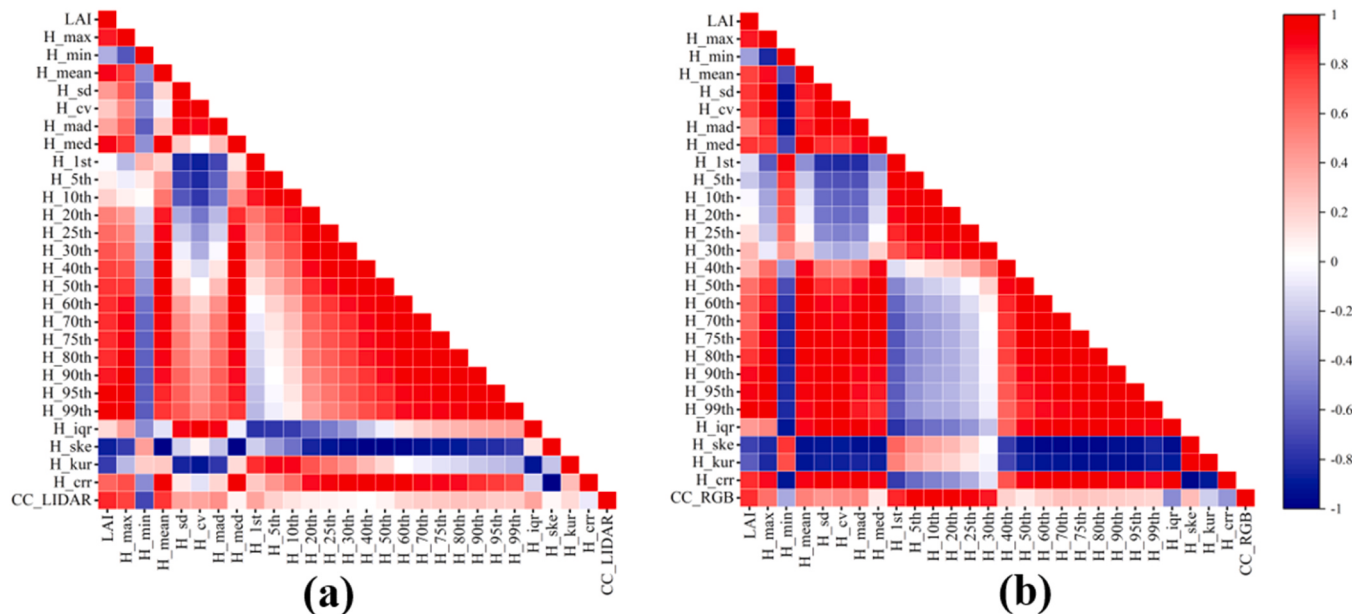


**Fig. 8.** Correlation coefficient between canopy structure metrics and LAI. (a) LiDAR-based canopy structure metrics. (b) RGB photogrammetry-based canopy structure metrics.

**Table 5**

Correlation coefficients between canopy structure indices and LAI for a single fertility period.

| Features            | June 30, 2023 |        | July 17, 2023 |        | August 23, 2023 |        | September 14, 2023 |        | September 30, 2023 |        |
|---------------------|---------------|--------|---------------|--------|-----------------|--------|--------------------|--------|--------------------|--------|
|                     | LiDAR         | RGB    | LiDAR         | RGB    | LiDAR           | RGB    | LiDAR              | RGB    | LiDAR              | RGB    |
| $H_{\max}$          | 0.725         | 0.753  | 0.772         | 0.781  | 0.845           | 0.798  | 0.891              | 0.843  | 0.752              | 0.773  |
| $H_{\min}$          | -0.422        | -0.326 | -0.301        | -0.333 | -0.489          | -0.376 | -0.562             | -0.386 | -0.433             | -0.435 |
| $H_{\text{mean}}$   | 0.820         | 0.729  | 0.840         | 0.735  | 0.813           | 0.755  | 0.890              | 0.779  | 0.801              | 0.709  |
| $H_{\text{sd}}$     | 0.395         | 0.677  | 0.473         | 0.723  | 0.359           | 0.786  | 0.429              | 0.780  | 0.373              | 0.692  |
| $H_{\text{cv}}$     | 0.221         | 0.660  | 0.209         | 0.722  | 0.257           | 0.763  | 0.262              | 0.793  | 0.266              | 0.704  |
| $H_{\text{mad}}$    | 0.331         | 0.445  | 0.353         | 0.523  | 0.392           | 0.545  | 0.373              | 0.537  | 0.322              | 0.492  |
| $H_{\text{med}}$    | 0.862         | 0.693  | 0.906         | 0.762  | 0.844           | 0.790  | 0.912              | 0.793  | 0.885              | 0.707  |
| $H_{1st}$           | -0.113        | -0.139 | -0.082        | -0.152 | -0.107          | -0.143 | -0.096             | -0.129 | -0.104             | -0.133 |
| $H_{5th}$           | 0.079         | -0.201 | 0.082         | -0.194 | 0.109           | -0.223 | 0.112              | -0.205 | 0.095              | -0.210 |
| $H_{10th}$          | 0.202         | -0.034 | 0.189         | -0.074 | 0.213           | -0.108 | 0.198              | -0.087 | 0.219              | -0.075 |
| $H_{20th}$          | 0.421         | 0.023  | 0.442         | 0.032  | 0.468           | 0.041  | 0.536              | 0.037  | 0.422              | 0.038  |
| $H_{25th}$          | 0.610         | 0.130  | 0.652         | 0.156  | 0.572           | 0.142  | 0.629              | 0.136  | 0.604              | 0.149  |
| $H_{30th}$          | 0.525         | 0.309  | 0.649         | 0.322  | 0.693           | 0.318  | 0.688              | 0.332  | 0.643              | 0.311  |
| $H_{40th}$          | 0.674         | 0.297  | 0.723         | 0.321  | 0.754           | 0.301  | 0.739              | 0.329  | 0.715              | 0.307  |
| $H_{50th}$          | 0.693         | 0.490  | 0.794         | 0.542  | 0.752           | 0.593  | 0.772              | 0.598  | 0.733              | 0.502  |
| $H_{60th}$          | 0.707         | 0.606  | 0.723         | 0.673  | 0.769           | 0.688  | 0.784              | 0.672  | 0.759              | 0.703  |
| $H_{70th}$          | 0.721         | 0.611  | 0.793         | 0.628  | 0.813           | 0.637  | 0.808              | 0.682  | 0.759              | 0.627  |
| $H_{75th}$          | 0.771         | 0.711  | 0.813         | 0.764  | 0.781           | 0.738  | 0.831              | 0.762  | 0.812              | 0.723  |
| $H_{80th}$          | 0.754         | 0.728  | 0.766         | 0.732  | 0.821           | 0.798  | 0.833              | 0.775  | 0.816              | 0.736  |
| $H_{90th}$          | 0.788         | 0.767  | 0.803         | 0.832  | 0.845           | 0.865  | 0.842              | 0.864  | 0.813              | 0.827  |
| $H_{95th}$          | 0.862         | 0.855  | 0.903         | 0.915  | 0.926           | 0.921  | 0.925              | 0.903  | 0.921              | 0.924  |
| $H_{99th}$          | 0.842         | 0.835  | 0.917         | 0.897  | 0.910           | 0.925  | 0.931              | 0.931  | 0.914              | 0.915  |
| $H_{lqr}$           | 0.163         | 0.233  | 0.152         | 0.335  | 0.167           | 0.433  | 0.192              | 0.440  | 0.183              | 0.338  |
| $H_{ske}$           | -0.821        | -0.724 | -0.836        | -0.731 | -0.864          | -0.723 | -0.869             | -0.729 | -0.851             | -0.721 |
| $H_{kur}$           | -0.678        | -0.628 | -0.642        | -0.602 | -0.728          | -0.617 | -0.713             | -0.648 | -0.702             | -0.637 |
| $H_{crr}$           | 0.527         | 0.715  | 0.595         | 0.742  | 0.622           | 0.813  | 0.647              | 0.802  | 0.614              | 0.822  |
| $CC_{\text{LiDAR}}$ | 0.722         |        | 0.826         | \      | 0.812           | \      | 0.806              | \      | 0.760              | \      |
| $CC_{\text{RGB}}$   | \             | 0.753  | \             | 0.734  | \               | 0.843  | \                  | 0.856  | \                  | 0.812  |

**Table 6**

Estimation results of a single-period data model based on canopy structure metrics.

| Date               | Metric         | DNN          |              | SVR   |       | RFR   |       | PLSR  |       |
|--------------------|----------------|--------------|--------------|-------|-------|-------|-------|-------|-------|
|                    |                | LiDAR        | RGB          | LiDAR | RGB   | LiDAR | RGB   | LiDAR | RGB   |
| June 30, 2023      | R <sup>2</sup> | <b>0.76</b>  | 0.65         | 0.71  | 0.63  | 0.73  | 0.63  | 0.71  | 0.61  |
|                    | RMSE           | <b>0.08</b>  | 0.12         | 0.16  | 0.13  | 0.14  | 0.13  | 0.17  | 0.13  |
|                    | RMSE%          | <b>8.47</b>  | 11.55        | 15.78 | 12.58 | 13.82 | 13.38 | 17.48 | 12.81 |
| July 17, 2023      | MAE            | <b>0.05</b>  | 0.09         | 0.12  | 0.10  | 0.11  | 0.08  | 0.08  | 0.10  |
|                    | R <sup>2</sup> | <b>0.77</b>  | 0.70         | 0.62  | 0.62  | 0.69  | 0.63  | 0.67  | 0.59  |
|                    | RMSE           | <b>0.41</b>  | 0.48         | 0.55  | 0.49  | 0.47  | 0.51  | 0.56  | 0.50  |
| August 23, 2023    | RMSE%          | <b>12.30</b> | 14.41        | 16.50 | 14.71 | 14.06 | 15.28 | 16.74 | 14.95 |
|                    | MAE            | <b>0.24</b>  | 0.41         | 0.27  | 0.35  | 0.52  | 0.49  | 0.41  | 0.33  |
|                    | R <sup>2</sup> | <b>0.76</b>  | 0.73         | 0.74  | 0.69  | 0.66  | 0.60  | 0.65  | 0.63  |
| September 14, 2023 | RMSE           | <b>0.43</b>  | 0.45         | 0.51  | 0.55  | 0.59  | 0.57  | 0.59  | 0.62  |
|                    | RMSE%          | <b>10.36</b> | 10.79        | 12.24 | 13.20 | 14.14 | 13.67 | 14.21 | 14.89 |
|                    | MAE            | <b>0.41</b>  | 0.30         | 0.31  | 0.28  | 0.42  | 0.34  | 0.32  | 0.47  |
| September 30, 2023 | R <sup>2</sup> | <b>0.81</b>  | 0.74         | 0.77  | 0.72  | 0.76  | 0.73  | 0.75  | 0.71  |
|                    | RMSE           | <b>0.39</b>  | 0.43         | 0.44  | 0.62  | 0.54  | 0.57  | 0.55  | 0.66  |
|                    | RMSE%          | <b>11.36</b> | 12.49        | 12.83 | 18.02 | 15.76 | 16.63 | 13.25 | 19.18 |
|                    | MAE            | <b>0.26</b>  | 0.37         | 0.33  | 0.48  | 0.36  | 0.32  | 0.41  | 0.43  |
|                    | R <sup>2</sup> | <b>0.72</b>  | <b>0.75</b>  | 0.70  | 0.74  | 0.67  | 0.73  | 0.61  | 0.70  |
|                    | RMSE           | <b>0.42</b>  | <b>0.39</b>  | 0.44  | 0.42  | 0.53  | 0.45  | 0.55  | 0.44  |
|                    | RMSE%          | <b>18.07</b> | <b>16.70</b> | 18.83 | 18.02 | 22.67 | 19.31 | 23.58 | 18.83 |
|                    | MAE            | <b>0.35</b>  | <b>0.27</b>  | 0.37  | 0.32  | 0.42  | 0.33  | 0.32  | 0.35  |

Note: The highlighted statistical figures represent the most accurate estimates of LAI obtained from data sources of a single period.

based on both sensors exceeding 70 %, and the RMSE% ranging from 11.36 % to 19.18 %. In the dataset from September 30, 2023, RGB photogrammetry-based metrics outperformed LiDAR-based metrics across all four models. This could be because of defoliation at the end of the cotton growth period, resulting in a thinner, simpler canopy structure, thereby enhancing the effectiveness of RGB photogrammetry in penetrating the canopy and capturing underlying features. The penetration capability of RGB photogrammetry is crucial for acquiring detailed information about the entire plant structure. RGB photogrammetry's high resolution and color information enable it to accurately capture these canopy changes. Conversely, LiDAR, primarily measuring canopy height and density, may be less sensitive to post-

defoliation changes in canopy structure. Following cotton defoliation, changes in canopy light conditions may lead to more detailed capture in RGB images. Consequently, RGB photogrammetry-derived canopy structure metrics might be more accurate. Therefore, it is concluded that LiDAR and RGB photogrammetry are differently impacted by canopy closure at various growth stages. In the early and middle stages with higher canopy closure, LiDAR's high penetration advantage enables the extraction of more structural features. Conversely, in later stages with reduced canopy closure, LiDAR's penetration advantage lessens, and RGB photogrammetry's high-resolution imaging can capture more detailed canopy structural features.

Fig. 9 shows the results of different models for LAI estimation at

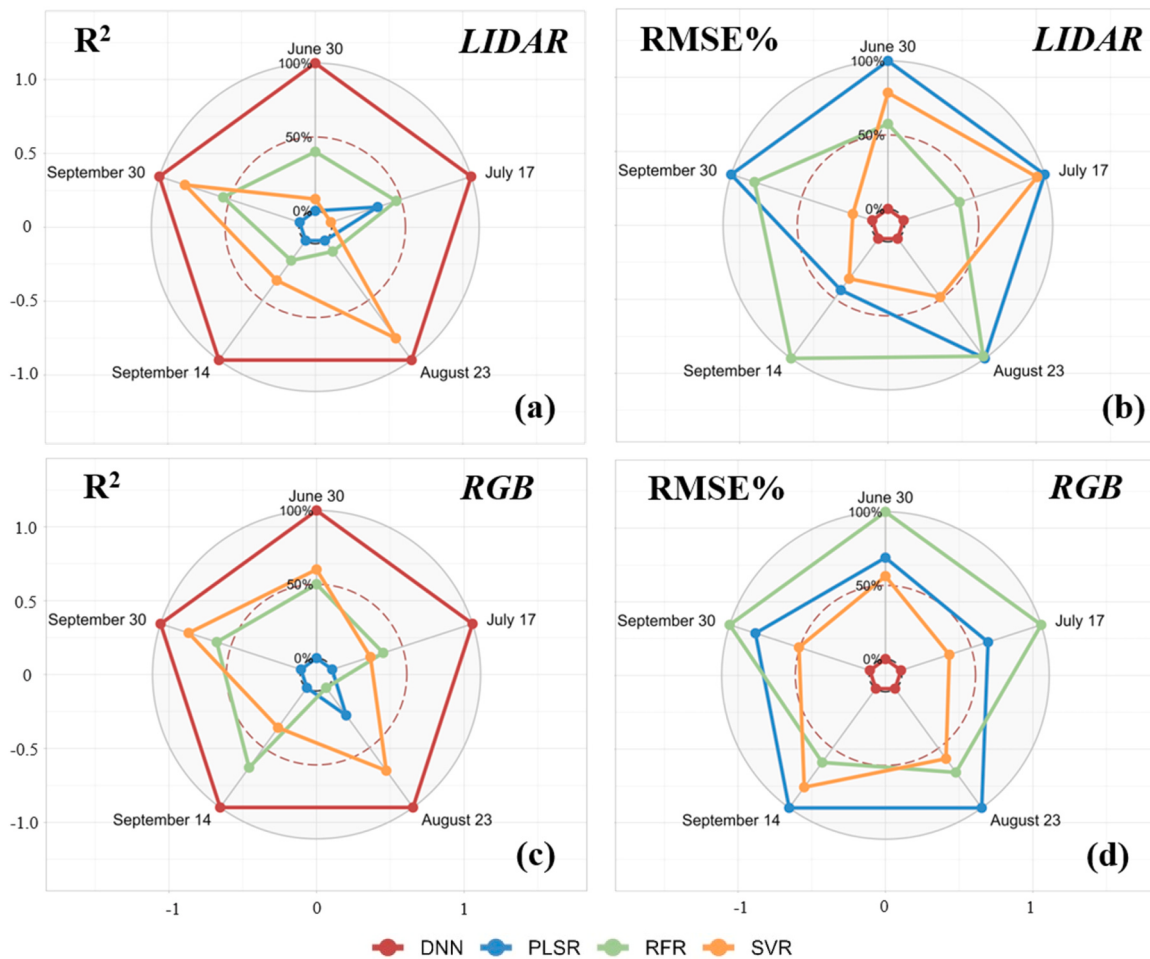


Fig. 9. The radar chart illustrating the accuracy evaluation of various models at different periods.

different fertility stages of cotton. The different colored lines in the figure represent different LAI estimation models; in the  $R^2$  plot, the closer the polygons connected by the lines are to the outer circle, the higher the prediction accuracy; in the RMSE plot, the closer the polygons connected by the lines are to the inner circle, the lower the estimation error.

Analysis of Fig. 9 reveals that DNN are the most effective algorithm for estimating cotton LAI, applicable to both LiDAR-based and RGB photogrammetry-based canopy structure metrics. DNN consistently shows the highest  $R^2$  values in every period and simultaneously exhibits lower RMSE% compared to other algorithms. The PLSR algorithm shows the poorest performance among all models, exhibiting the lowest  $R^2$  in most periods and higher RMSE% values. While machine learning models generally perform better on large datasets, they may struggle to uncover deep connections within small sample sizes (96), impacting their generalization capabilities. Despite this, DNNs can autonomously learn complex features through multi-layer representation learning. This ability enables DNNs to extract substantial information from each sample in small datasets, potentially enhancing the model's predictive capability (Liu et al., 2021). The characteristics of the cotton canopy vary significantly over time. The adaptability and generalization capabilities of DNN enable it to maintain robust performance in these dynamic environments. Furthermore, the deep architecture of DNN, characterized by multiple nonlinear transformation layers, facilitates the abstraction of data. This feature aids in capturing elusive patterns within limited data, thereby enhancing DNN's performance in predicting cotton LAI for individual periods.

#### 4.3. Estimation of cotton LAI at all growth stages separately using multiple sensors

The performance of LiDAR-based canopy structure metrics and RGB photogrammetry-based canopy structure metrics were trained and validated together at all growth stages, while at the same time spectral features and texture features extracted from multispectral images of UAVs at all growth stages were combined and trained and validated together, and the models constructed based on these three sensors were compared. The evaluation results of the models are shown in Table 7.

The results indicated that LiDAR-based canopy structure metrics outperformed RGB photogrammetry-based metrics across all growth stages, exhibiting an average  $R^2$  increase of 0.03 and an average RMSE% decrease of 0.75 % across the four models. Furthermore, the highest accuracy was attained with multispectral image features as model inputs, yielding an average  $R^2$  of 0.71 and an average RMSE% of 16.78 % for the four models. This suggests that the spectral and textural information from multispectral data is vital for accurate LAI estimation in vegetation, enhancing the models' ability to estimate LAI. The spectral features of multispectral images capture vegetation reflectance across various bands, with each band's information closely linked to the plants' biochemical properties. Texture features offer detailed insights into the vegetation surface, depicting spatial arrangement and pixel variation patterns in the image, which correspond to the vegetation's spatial distribution and growth. This textural information aids in understanding canopy density and heterogeneity, crucial for accurate LAI estimation. Compared to canopy structure metrics, the spectral and textural features of multispectral images may offer more direct information related to

**Table 7**

Evaluation results for the estimation of cotton LAI at all growth stages using various sensors.

| Sensor Type | Feature Type | No. of features | Metric | DNN          | SVR   | RFR   | PLSR  |
|-------------|--------------|-----------------|--------|--------------|-------|-------|-------|
| LiDAR       | SM           | 27              | $R^2$  | <b>0.74</b>  | 0.70  | 0.67  | 0.60  |
|             |              |                 | RMSE   | <b>0.45</b>  | 0.47  | 0.48  | 0.50  |
|             |              |                 | RMSE%  | <b>14.49</b> | 16.72 | 17.67 | 22.02 |
|             |              |                 | MAE    | <b>0.33</b>  | 0.35  | 0.38  | 0.37  |
| RGB         | SM           | 27              | $R^2$  | <b>0.70</b>  | 0.64  | 0.64  | 0.61  |
|             |              |                 | RMSE   | <b>0.47</b>  | 0.49  | 0.50  | 0.52  |
|             |              |                 | RMSE%  | <b>15.18</b> | 17.40 | 18.44 | 22.90 |
|             |              |                 | MAE    | <b>0.35</b>  | 0.39  | 0.38  | 0.39  |
| MS          | SF+TF        | 68              | $R^2$  | <b>0.77</b>  | 0.72  | 0.70  | 0.66  |
|             |              |                 | RMSE   | <b>0.40</b>  | 0.44  | 0.47  | 0.48  |
|             |              |                 | RMSE%  | <b>12.96</b> | 15.63 | 17.34 | 21.19 |
|             |              |                 | MAE    | <b>0.29</b>  | 0.33  | 0.36  | 0.34  |

Note: SM represents Structure-based Metrics, SF represents Spectral Features, and TF represents Texture Features. The highlighted statistical figures represent the most accurate estimates of LAI obtained from data sources of all growth stages.

LAI. Additionally, the DNN model emerged as the most effective for LAI prediction across all three sensors. DNNs were capable of capturing the intricate relationship between vegetation features and LAI by learning complex data representations from extensive datasets spanning multiple periods.

#### 4.4. Fusion of canopy structure metrics with multispectral image-based features to estimate cotton LAI

The LiDAR-based canopy structure indexes and RGB photogrammetry-based canopy structure indexes with spectral features extracted from multispectral images were fused with texture features for all growth stages, respectively. The evaluation results of each model are shown in Table 8.

The results indicated an improvement in LAI prediction accuracy when fusing LiDAR-based and RGB photogrammetry-based canopy structure metrics, as opposed to relying solely on multispectral spectral and texture features (Table 7). Post-fusion, the average  $R^2$  for the four models increased by 0.05 and the average RMSE% decreased by 4.7 % for LiDAR-based metrics. Similarly, for RGB photogrammetry-based metrics, the average  $R^2$  increased by 0.0225, and the average RMSE% decreased by 3.43 %. Canopy structure features from RGB and LiDAR images provide independent insights into canopy growth and structure. Fusing these features with those extracted from passive sensors addresses, to some extent, the asymptotic saturation problem inherent in passive sensors, aligning with prior research (Bendig et al., 2015; Stanton et al., 2017). Concurrently, the DNN remains the top-performing model. Full-period multi-class feature fusion, encapsulating data from various time points, enables DNN to effectively capture the dynamic processes of vegetation growth and change. DNNs can autonomously learn and extract complex features through their multiple hidden layers. This capability allows them to delve into the underlying patterns and features within multi-class feature fusion inputs, resulting in a more accurate reflection of LAI. The training and validation results for each model, post-feature fusion, are presented in Fig. 10.

**Table 8**

Evaluation results for the estimation of maize LAI at all growth stages using multimodal fusion data.

| Sensor Type | Feature Type | No. of features | Metric | DNN          | SVR   | RFR   | PLSR  |
|-------------|--------------|-----------------|--------|--------------|-------|-------|-------|
| LiDAR+MS    | SM+ SF+TF    | 95              | $R^2$  | <b>0.84</b>  | 0.77  | 0.74  | 0.70  |
|             |              |                 | RMSE   | <b>0.34</b>  | 0.41  | 0.44  | 0.46  |
|             |              |                 | RMSE%  | <b>9.94</b>  | 12.01 | 12.91 | 13.46 |
|             |              |                 | MAE    | <b>0.27</b>  | 0.31  | 0.34  | 0.33  |
| RGB+MS      | SM+ SF+TF    | 95              | $R^2$  | <b>0.80</b>  | 0.74  | 0.72  | 0.68  |
|             |              |                 | RMSE   | <b>0.38</b>  | 0.43  | 0.44  | 0.47  |
|             |              |                 | RMSE%  | <b>11.82</b> | 13.34 | 13.64 | 14.61 |
|             |              |                 | MAE    | <b>0.29</b>  | 0.32  | 0.35  | 0.34  |

Note: SM represents Structure-based Metrics, SF represents Spectral Features, and TF represents Texture Features. The highlighted statistical figures represent the most accurate estimates of LAI obtained from data sources of all growth stages.

#### 4.5. Interpretability analysis of inversion DNN model based on SHAP method

In this study, SHAP was used to analyze the properties of the DNN models that performed best in predicting LAI in cotton. To assess the significance of various features from each sensor in predicting cotton LAI, this study fused LiDAR-based and RGB photogrammetry-based canopy structure metrics from the full-growth stage with spectral and texture features from multispectral images. These combined features were then input into the DNN, utilizing SHAP to quantify each feature's contribution to the prediction. The performance of the DNN model, using these two datasets, is displayed in Fig. 11, organized in descending order of mean absolute SHAP value. For convenience, only the top 20 most influential features in each dataset are presented.

As indicated in Fig. 11(b) and (d), texture features derived from UAV multispectral imagery were paramount in predicting cotton LAI. These features comprised over half of the top 20 most important features and ranked highest in importance among both dataset inputs. The significance of these texture features surpassed that of spectral features, as well as LiDAR-based and RGB photogrammetry-based canopy structure metrics. Despite most canopy structure metrics from both LiDAR and RGB photogrammetry demonstrating high correlations with LAI (as seen in Fig. 8), only a select few were deemed important in the actual model construction for LAI estimation. This observation may stem from the algorithm's approach to feature importance assessment, which involves evaluating not just the individual contributions of each variable but also their multivariate interactions with others. Consequently, if multiple variables are correlated (covariate) with each other, they may be assigned less importance due to potential redundancy in their predictive information within the model.

Identifying the most influential features and their patterns of influence is a key objective of this study, hence the focus on the scatter distribution of SHAP values. In Fig. 11(a) and (c), the color intensity of the dots indicates feature value magnitude. Dots on the right side of the horizontal axis represent a positive contribution (increasing the

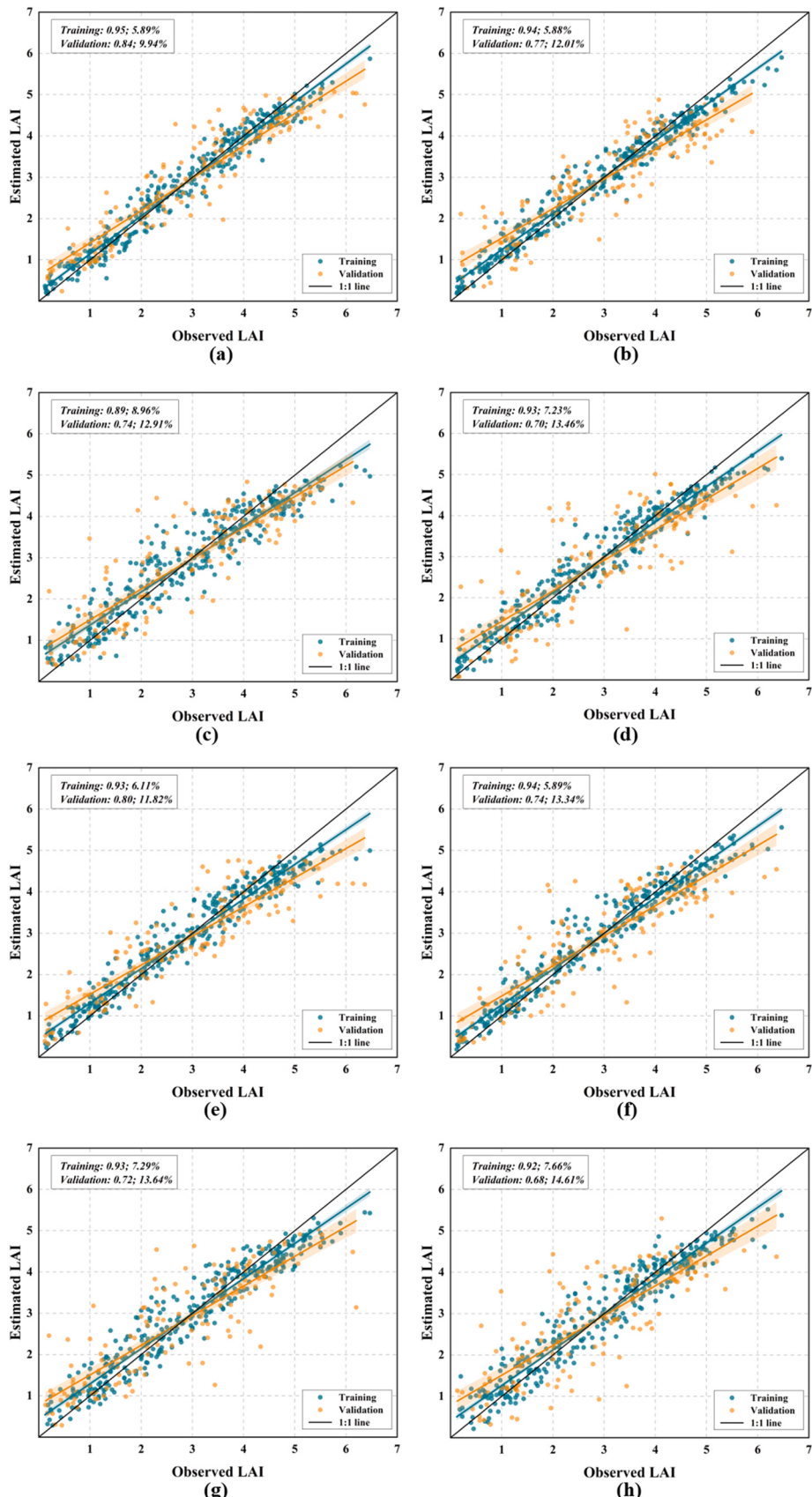


**Fig. 10.** The results of training and validating the LAI prediction model with multimodal data fusion throughout the all growth stages. Note: (a-d) are model evaluations of DNN, SVR, RFR, and PLSR after fusion of LiDAR with multispectral features, and (e-h) are model evaluations of DNN, SVR, RFR, and PLSR after fusion of RGB with multispectral features.

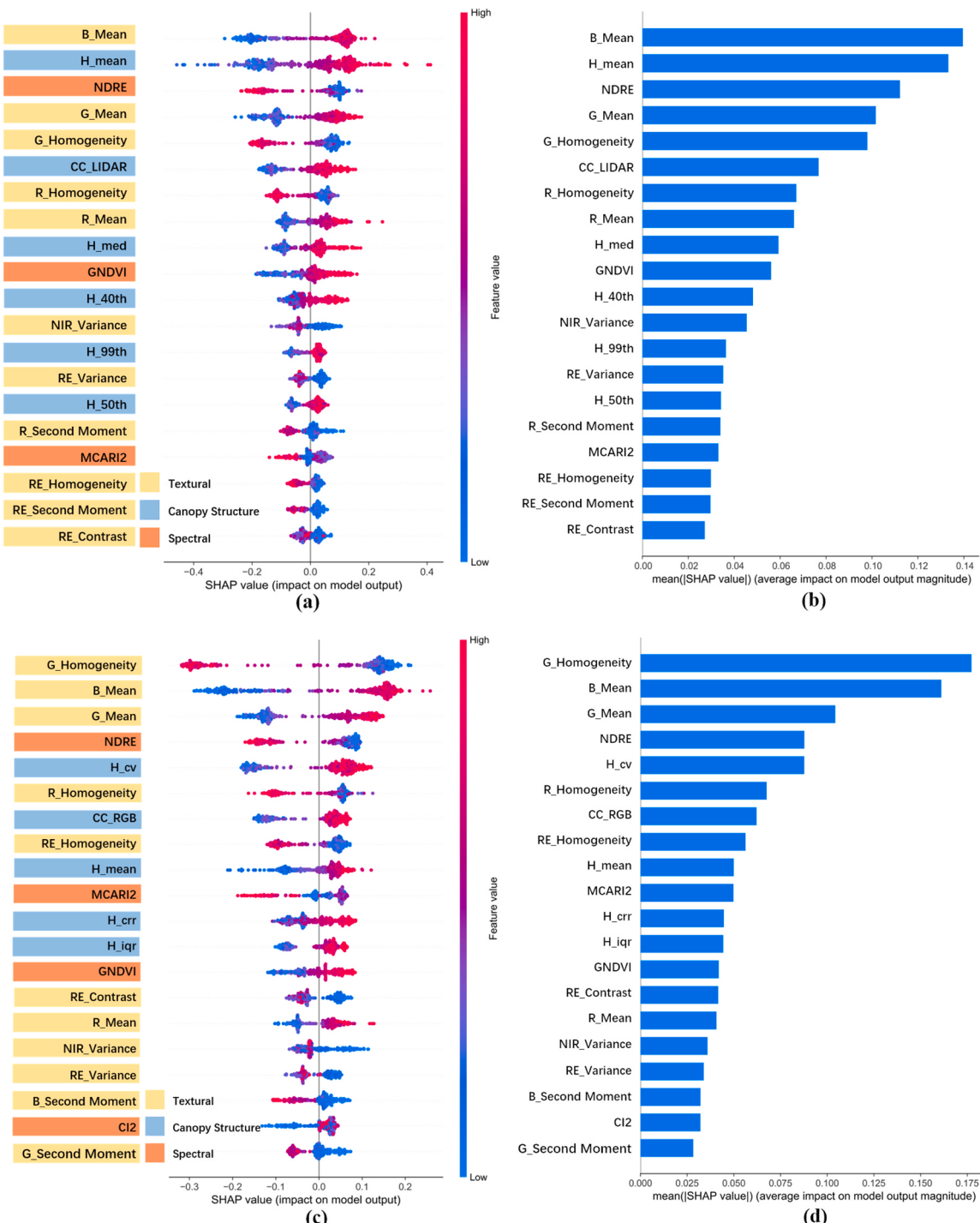


**Fig. 11.** (a-b) SHAP evaluation of DNN model after fusion of LiDAR and multispectral data, (c-d) SHAP evaluation of DNN model after fusion of RGB and multispectral data.

predicted value), while those on the left side indicate a negative contribution (decreasing the predicted value). Features spanning a wider area on the plot suggest a more significant impact on the model output. Specifically, texture features *B\_Mean* and *G\_Mean*, ranked in the top five for both feature combinations, exhibit similar influence patterns on predicted values. Higher *B\_Mean* or *G\_Mean* values tend to increase the model's predicted values. In contrast, the texture feature *G\_Homogeneity*, also ranked in the top five, influences predicted values differently. Higher *G\_Homogeneity* values tend to decrease the model's predicted values.

In terms of structural metrics for the canopy from both sources, *H\_mean* and *CC* showed superior performance, both ranking in the top ten. The influence patterns indicated that higher eigenvalues correlated with increased predictive values of the model. Among the spectral indices of multispectral images, the *NDRE* exhibited the most significant influence on the model, with lower *NDRE* values corresponding to increased predicted values. Although the *MCARI2* ranks among the top 20 in both datasets, its distribution pattern is unclear. In the SHAP results, the mixture of red and blue scatters within the range of positive SHAP values suggests low reliability of *MCARI2* features with cotton LAI.

#### 4.6. Mapping cotton LAI

Estimates of cotton LAI from September 14, 2023 were selected to map the spatial distribution of LAI using a dataset based on two sources of canopy structure metrics fused with multispectral image features, respectively, to construct a DNN model, and based on the model's predictions to map the spatial distribution of cotton LAI maps, which are shown in Fig. 12.

Analysis of the spatial distribution map, depicting cotton LAI as predicted by the DNN model, reveals that LAI values in the N0 region (with 0 kg/hm<sup>2</sup> nitrogen application) are lower compared to regions with nitrogen fertilizer application, with most LAI values in N0 being below 2.0. In contrast, regions N1, N2, and N3, which received standard and enhanced nitrogen fertilizer treatments, predominantly had predicted LAI values above 2.0. This observation suggests that severe nitrogen deficiency significantly impacts the growth and development of cotton.

#### 5. Conclusions

This study evaluated the effectiveness of canopy structure metrics derived from UAV LiDAR and RGB photogrammetry for LAI prediction in cotton across all fertility stages. It also compared machine learning and deep learning approaches by integrating spectral and texture features from UAV multispectral images. The main conclusions of the study are as follows:

1. Canopy structure metrics derived from UAV LiDAR and photogrammetry exhibited varying performances at different fertility stages, attributable to the degrees of canopy closure.
2. Models using multimodal data (RGB + MS or LiDAR + MS) outperformed unimodal data models. The integration of LiDAR-based canopy structure metrics with multispectral image features resulted in higher prediction accuracy and more robust models.
3. The DNN-based LAI prediction model surpassed the performance of PLSR, SVR, and RFR methods.
4. In the DNN-based LAI prediction model with multimodal data input, texture features emerged as the most significant.

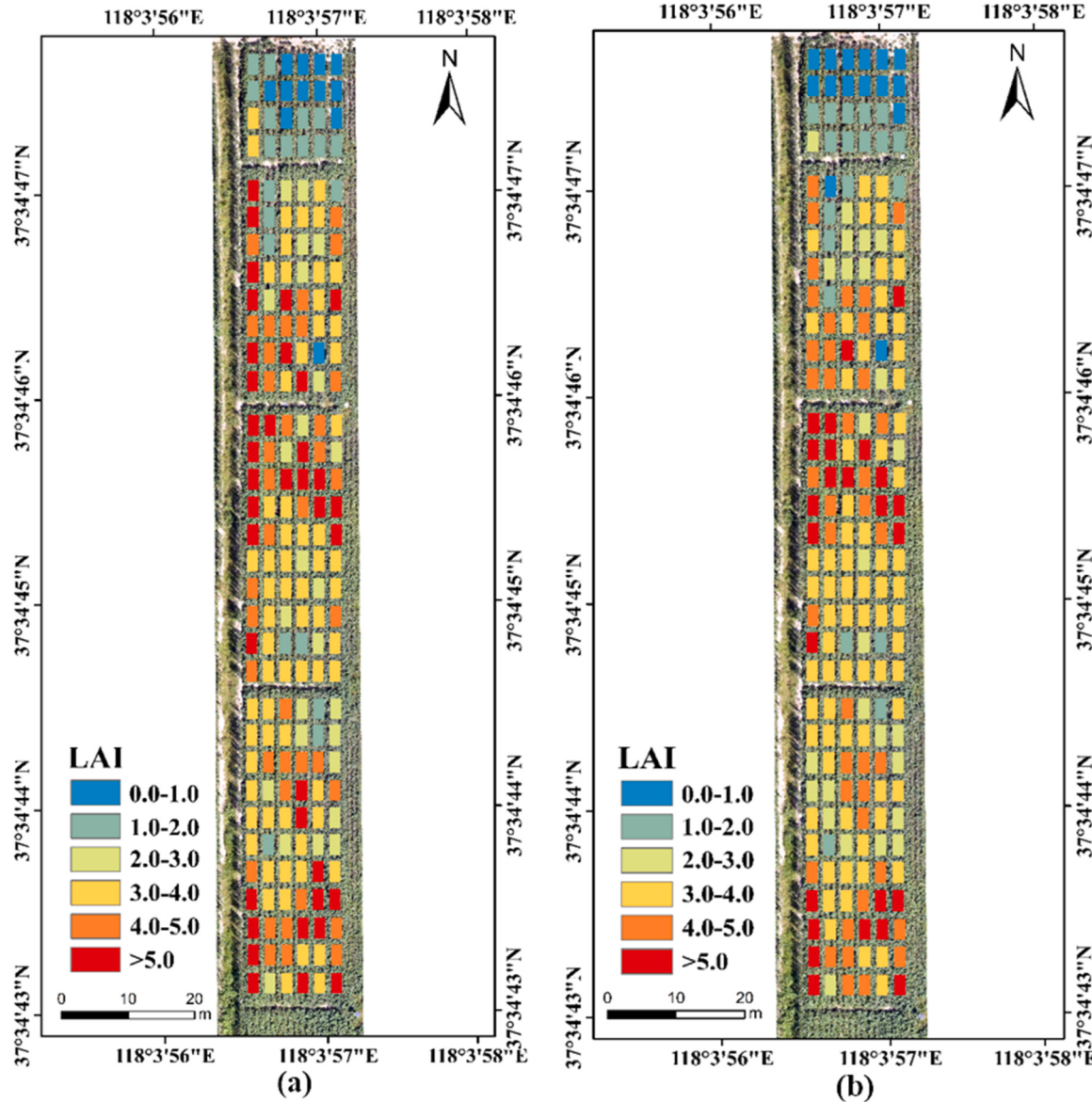


**Fig. 12.** (a) The spatial distribution of LAI predicted by the DNN model fused with LiDAR and multispectral data, (b) The spatial distribution of LAI predicted by the DNN model fused with RGB and multispectral data.

The findings of this study demonstrate significant potential for UAV multisensor-based LAI prediction using multimodal data fusion and DNN methods. However, to further evaluate the robustness of this approach, it is necessary to test multiple genotypes across various crop types, developmental stages, and environmental conditions. At the same time, due to the single source of ground-measured LAI (only using the Sunscan plant canopy analyzer), whether this will limit the prediction accuracy of multi-modal data requires further research.

### CRediT authorship contribution statement

**Lechun Zhang:** Writing – original draft, Investigation, Conceptualization. **Binshu Sun:** Validation, Investigation. **Denan Zhao:** Investigation, Data curation. **Changfeng Shan:** Software. **Baoju Wang:** Investigation. **Guobin Wang:** Resources. **Can-can Song:** Resources. **Pengchao Chen:** Writing – review & editing, Methodology. **Yubin Lan:** Supervision, Resources, Funding acquisition.

### Declaration of Competing Interest

The authors declare that they have no known competing financial interests or personal relationships that could have appeared to influence the work reported in this paper.

### Data availability

Data will be made available on request.

### Acknowledgment

This research was supported by the National Natural Science Foundation of China (32302410), National Natural Science Foundation of China (32301716), Ningxia key research and development plan (2023BCF01051), Natural Science Foundation of Shandong Province (ZR2021QC154), China Agriculture Research System (CARS-15-22), National Key R&D Program of China (2023YFD2000200).

### References

- Alton, P.B., 2016. The sensitivity of models of gross primary productivity to meteorological and leaf area forcing: A comparison between a Penman–Monteith ecophysiological approach and the MODIS Light-Use Efficiency algorithm. *Agric. Meteorol.* 218, 11–24. <https://doi.org/10.1016/j.agrformet.2015.11.010>.
- Asner, G.P., Braswell, B., Schimel, D.S., Wessman, C.A., 1998. Ecological research needs from multiangle remote sensing data. *Remote Sens. Environ.* 63, 155–165. [https://doi.org/10.1016/S0034-4257\(97\)00139-9](https://doi.org/10.1016/S0034-4257(97)00139-9).
- Ball, J.E., Anderson, D.T., Chan, C.S., 2017. Comprehensive survey of deep learning in remote sensing: theories, tools, and challenges for the community, 042609-042609. *J. Appl. Remote Sens.* 11. <https://doi.org/10.1117/1.JRS.11.042609>.
- Baret, F., Guyot, G., 1991. Potentials and limits of vegetation indices for LAI and APAR assessment. *Remote Sens. Environ.* 35, 161–173. [https://doi.org/10.1016/0034-4257\(91\)90009-U](https://doi.org/10.1016/0034-4257(91)90009-U).
- Bendig, J., Yu, K., Aasen, H., Bolten, A., Bennertz, S., Broscheit, J., Gnyp, M.L., Bareth, G., 2015. Combining UAV-based plant height from crop surface models, visible, and near infrared vegetation indices for biomass monitoring in barley. *Int. J. Appl. Earth Obs. Geoinf.* 39, 79–87. <https://doi.org/10.1016/j.jag.2015.02.012>.
- Bréda, N.J., 2003. Ground-based measurements of leaf area index: a review of methods, instruments and current controversies. *J. Exp. Bot.* 54, 2403–2417. <https://doi.org/10.1093/jxb/erg263>.
- Broge, N.H., Leblanc, E., 2001. Comparing prediction power and stability of broadband and hyperspectral vegetation indices for estimation of green leaf area index and canopy chlorophyll density. *Remote Sens. Environ.* 76, 156–172. [https://doi.org/10.1016/S0034-4257\(00\)00197-8](https://doi.org/10.1016/S0034-4257(00)00197-8).
- Cai, Y., Guan, K., Peng, J., Wang, S., Seifert, C., Wardlow, B., Li, Z., 2018. A high-performance and in-season classification system of field-level crop types using time-series Landsat data and a machine learning approach. *Remote Sens. Environ.* 210, 35–47. <https://doi.org/10.1016/j.rse.2018.02.045>.
- Camacho, F., Cernicharo, J., Lacaze, R., Baret, F., Weiss, M., 2013. GEOV1: LAI, FAPAR essential climate variables and FCOVER global time series capitalizing over existing products. Part 2: Validation and intercomparison with reference products. *Remote Sens. Environ.* 137, 310–329. <https://doi.org/10.1016/j.rse.2013.02.030>.
- Camps-Valls, G., Campos-Taberner, M., Moreno-Martínez, Á., Walther, S., Duveiller, G., Cescatti, A., Mahecha, M.D., Muñoz-Marí, J., García-Haro, F.J., Guanter, L., 2021. A unified vegetation index for quantifying the terrestrial biosphere. *Sci. Adv.* 7, eabc7447. <https://doi.org/10.1126/sciadv.abc7447>.
- Chen, J.M., 1996. Evaluation of vegetation indices and a modified simple ratio for boreal applications. *Can. J. Remote Sens.* 22, 229–242. <https://doi.org/10.1080/07038992.1996.10855178>.
- Chen, P., Xu, W., Zhan, Y., Wang, G., Yang, W., Lan, Y., 2022. Determining application volume of unmanned aerial spraying systems for cotton defoliation using remote sensing images. *Comput. Electron. Agric.* 196, 106912. <https://doi.org/10.1016/j.compag.2022.106912>.
- Colomina, I., Molina, P., 2014. Unmanned aerial systems for photogrammetry and remote sensing: A review. *ISPRS J. Photogramm. Remote Sens.* 92, 79–97. <https://doi.org/10.1016/j.isprsjprs.2014.02.013>.
- Dandois, J.P., Ellis, E.C., 2013. High spatial resolution three-dimensional mapping of vegetation spectral dynamics using computer vision. *Remote Sens. Environ.* 136, 259–276. <https://doi.org/10.1016/j.rse.2013.04.005>.
- Datt, B., 1999. A new reflectance index for remote sensing of chlorophyll content in higher plants: tests using Eucalyptus leaves. *J. Plant Physiol.* 154, 30–36. [https://doi.org/10.1016/S0176-1617\(99\)80314-9](https://doi.org/10.1016/S0176-1617(99)80314-9).
- Daughtry, C.S., Walther, C., Kim, M., De Colstoun, E.B., McMurtrey II, J., 2000. Estimating corn leaf chlorophyll concentration from leaf and canopy reflectance. *Remote Sens. Environ.* 74, 229–239. [https://doi.org/10.1016/S0176-1617\(99\)80314-9](https://doi.org/10.1016/S0176-1617(99)80314-9).
- Dechant, B., Ryu, Y., Badgley, G., Zeng, Y., Berry, J.A., Zhang, Y., Goulas, Y., Li, Z., Zhang, Q., Kang, M., 2020. Canopy structure explains the relationship between photosynthesis and sun-induced chlorophyll fluorescence in crops. *Remote Sens. Environ.* 241, 111733. <https://doi.org/10.1016/j.rse.2020.111733>.
- Durbha, S.S., King, R.L., Younan, N.H., 2007. Support vector machines regression for retrieval of leaf area index from multiangle imaging spectroradiometer. *Remote Sens. Environ.* 107, 348–361. <https://doi.org/10.1016/j.rse.2006.09.031>.
- Duursma, R.A., Gimeno, T.E., Boer, M.M., Crous, K.Y., Tjoelker, M.G., Ellsworth, D.S., 2016. Canopy leaf area of a mature evergreen Eucalyptus woodland does not respond to elevated atmospheric [CO<sub>2</sub>] but tracks water availability. *Glob. Change Biol.* 22, 1666–1676. <https://doi.org/10.1111/gcb.13151>.
- Fang, H., Baret, F., Plummer, S., Schaepman-Strub, G., 2019. An overview of global leaf area index (LAI): Methods, products, validation, and applications. *Rev. Geophys.* 57, 739–799. <https://doi.org/10.1029/2018RG000608>.
- Ganguly, S., Schull, M.A., Samanta, A., Shabanov, N.V., Milesi, C., Nemani, R.R., Knyazikhin, Y., Myeni, R.B., 2008. Generating vegetation leaf area index earth system data record from multiple sensors. Part 1: Theory. *Remote Sens. Environ.* 112, 4333–4343. <https://doi.org/10.1016/j.rse.2008.07.014>.
- Gitelson, A.A., Kaufman, Y.J., Merzlyak, M.N., 1996. Use of a green channel in remote sensing of global vegetation from EOS-MODIS. *Remote Sens. Environ.* 58, 289–298. [https://doi.org/10.1016/S0034-4257\(96\)00072-7](https://doi.org/10.1016/S0034-4257(96)00072-7).
- Gitelson, A., Merzlyak, M.N., 1994. Quantitative estimation of chlorophyll-a using reflectance spectra: Experiments with autumn chestnut and maple leaves. *J. Photochem. Photobiol. B* 22, 247–252. [https://doi.org/10.1016/1011-1344\(93\)06963-4](https://doi.org/10.1016/1011-1344(93)06963-4).
- Gitelson, A.A., Merzlyak, M.N., 1996. Signature analysis of leaf reflectance spectra: algorithm development for remote sensing of chlorophyll. *J. Plant Physiol.* 148, 494–500. [https://doi.org/10.1016/S0176-1617\(96\)80284-7](https://doi.org/10.1016/S0176-1617(96)80284-7).
- Gitelson, A.A., Merzlyak, M.N., 1997. Remote estimation of chlorophyll content in higher plant leaves. *Int. J. Remote Sens.* 18, 2691–2697. <https://doi.org/10.1080/014311697217558>.
- Gitelson, A.A., Peng, Y., Arkebauer, T.J., Schepers, J., 2014. Relationships between gross primary production, green LAI, and canopy chlorophyll content in maize: Implications for remote sensing of primary production. *Remote Sens. Environ.* 144, 65–72. <https://doi.org/10.1016/j.rse.2014.01.004>.
- Gitelson, A.A., Viña, A., Arkebauer, T.J., Rundquist, D.C., Keydan, G., Leavitt, B., 2003. Remote estimation of leaf area index and green leaf biomass in maize canopies. *Geophys. Res. Lett.* 30. <https://doi.org/10.1029/2002GL016450>.
- Goel, N.S., Qin, W., 1994. Influences of canopy architecture on relationships between various vegetation indices and LAI and FPAR: A computer simulation. *Remote Sensing Reviews* 10, 309–347. <https://doi.org/10.1080/02757259409532252>.
- Gower, S.T., Kucharik, C.J., Norman, J.M., 1999. Direct and indirect estimation of leaf area index, FAPAR, and net primary production of terrestrial ecosystems. *Remote Sens. Environ.* 70, 29–51. [https://doi.org/10.1016/S0034-4257\(99\)00056-5](https://doi.org/10.1016/S0034-4257(99)00056-5).
- Haboudane, D., Miller, J.R., Pattee, E., Zarco-Tejada, P.J., Strachan, I.B., 2004. Hyperspectral vegetation indices and novel algorithms for predicting green LAI of crop canopies: Modeling and validation in the context of precision agriculture. *Remote Sens. Environ.* 90, 337–352. <https://doi.org/10.1016/j.rse.2003.12.013>.
- Haboudane, D., Miller, J.R., Tremblay, N., Zarco-Tejada, P.J., Dextraze, L., 2002. Integrated narrow-band vegetation indices for prediction of crop chlorophyll content for application to precision agriculture. *Remote Sens. Environ.* 81, 416–426. [https://doi.org/10.1016/S0034-4257\(02\)00018-4](https://doi.org/10.1016/S0034-4257(02)00018-4).
- Haralick, R.M., Shanmugam, K., Dinstein, I.H., 1973. Textural features for image classification. *IEEE Trans. Syst., Man, Cybern.* 610–621. <https://doi.org/10.1109/TSMC.1973.4309314>.
- Houborg, R., McCabe, M.F., 2018. A hybrid training approach for leaf area index estimation via Cubist and random forests machine-learning. *ISPRS J. Photogramm. Remote Sens.* 135, 173–188. <https://doi.org/10.1016/j.isprsjprs.2017.10.004>.
- Houldcroft, C.J., Campbell, C.L., Davenport, I.J., Gurney, R.J., Holden, N., 2005. Measurement of canopy geometry characteristics using LiDAR laser altimetry: A feasibility study. *IEEE Trans. Geosci. Remote Sens.* 43, 2270–2282. <https://doi.org/10.1109/TGRS.2005.856639>.
- Huete, A.R., 1988. A soil-adjusted vegetation index (SAVI). *Remote Sens. Environ.* 25, 295–309. [https://doi.org/10.1016/0034-4257\(88\)90106-X](https://doi.org/10.1016/0034-4257(88)90106-X).

- Huete, A., Didan, K., Miura, T., Rodriguez, E.P., Gao, X., Ferreira, L.G., 2002. Overview of the radiometric and biophysical performance of the MODIS vegetation indices. *Remote Sens. Environ.* 83, 195–213. [https://doi.org/10.1016/S0034-4257\(02\)00096-2](https://doi.org/10.1016/S0034-4257(02)00096-2).
- J. Dash P. Curran The MERIS terrestrial chlorophyll index 2004 doi: 10.1080/0143116042000274015.
- Jin, S., Sun, X., Wu, F., Su, Y., Li, Y., Song, S., Xu, K., Ma, Q., Baret, F., Jiang, D., 2021. Lidar sheds new light on plant phenomics for plant breeding and management: Recent advances and future prospects. *ISPRS J. Photogramm. Remote Sens.* 171, 202–223 <http://doi.org/j.isprsjrs.2020.11.006>.
- Jonckheere, I., Fleck, S., Nackaerts, K., Muys, B., Coppin, P., Weiss, M., Baret, F., 2004. Review of methods for in situ leaf area index determination: Part I. Theories, sensors and hemispherical photography. *Agric. Meteorol.* 121, 19–35. <https://doi.org/10.1016/j.agrformet.2003.08.027>.
- Kaufman, Y.J., Tanre, D., 1992. Atmospherically resistant vegetation index (ARVI) for EOS-MODIS. *IEEE Trans. Geosci. Remote Sens.* 30, 261–270. <https://doi.org/10.1109/36.134076>.
- Kimura, R., Okada, S., Miura, H., Kamichika, M., 2004. Relationships among the leaf area index, moisture availability, and spectral reflectance in an upland rice field. *Agric. Water Manag.* 69, 83–100. <https://doi.org/10.1016/j.agwat.2004.04.009>.
- Koetz, B., Baret, F., Poilv  , H., Hill, J., 2005. Use of coupled canopy structure dynamic and radiative transfer models to estimate biophysical canopy characteristics. *Remote Sens. Environ.* 95, 115–124. <https://doi.org/10.1016/j.rse.2004.11.017>.
- Lan, Y., Shengde, C., Fritz, B.K., 2017. Current status and future trends of precision agricultural aviation technologies. *Int. J. Agric. Biol. Eng.* 10, 1–17. <https://doi.org/10.3965/j.ijabe.20171003.3088>.
- Li, F., Mistele, B., Hu, Y., Yue, X., Yue, S., Miao, Y., Chen, X., Cui, Z., Meng, Q., Schmidhalter, U., 2012. Remotely estimating aerial N status of phenologically differing winter wheat cultivars grown in contrasting climatic and geographic zones in China and Germany. *Field Crops Res* 138, 21–32. <https://doi.org/10.1016/j.fcr.2012.09.002>.
- Li, W., Niu, Z., Wang, C., Huang, W., Chen, H., Gao, S., Li, D., Muhammad, S., 2015. Combined use of airborne LiDAR and satellite GF-1 data to estimate leaf area index, height, and aboveground biomass of maize during peak growing season. *IEEE J. Sel. Top. Appl. Earth Obs. Remote Sens.* 8, 4489–4501. <https://doi.org/10.1109/JSTARS.2015.2496358>.
- Li, K., Dong, X., Qiu, B., 2020. Analysis of cotton height spatial variability based on UAV-LiDAR. *Int. J. Precis. Agric. Aviat.* 3 <https://doi.org/10.33440/j.ijpaa.20200303.79>.
- Liu, S., Jin, X., Bai, Y., Wu, W., Cui, N., Cheng, M., Liu, Y., Meng, L., Jia, X., Nie, C., 2023. UAV multispectral images for accurate estimation of the maize LAI considering the effect of soil background. *Int. J. Appl. Earth Obs. Geoinf.* 121, 103383 <https://doi.org/10.1016/j.jag.2023.103383>.
- Liu, S., Jin, X., Nie, C., Wang, S., Yu, X., Cheng, M., Shao, M., Wang, Z., Tuohuti, N., Bai, Y., 2021. Estimating leaf area index using unmanned aerial vehicle data: shallow vs. deep machine learning algorithms. *Plant Physiol.* 187, 1551–1576. <https://doi.org/10.1093/plphys/kiab322>.
- L  udeke, M., Janecek, A., Kohlmaier, G.H., 1991. Modelling the seasonal CO<sub>2</sub> uptake by land vegetation using the global vegetation index. *Tellus B* 43, 188–196. <https://doi.org/10.1034/j.1600-0889.1991.00012.x>.
- Luo, S., Chen, J.M., Wang, C., Gonsamo, A., Xi, X., Lin, Y., Qian, M., Peng, D., Nie, S., Qin, H., 2017. Comparative performances of airborne LiDAR height and intensity data for leaf area index estimation. *IEEE J. Sel. Top. Appl. Earth Obs. Remote Sens.* 11, 300–310. <https://doi.org/10.1109/JSTARS.2017.2765890>.
- Ma, Q., Su, Y., Guo, Q., 2017. Comparison of canopy cover estimations from airborne LiDAR, aerial imagery, and satellite imagery. *IEEE J. Sel. Top. Appl. Earth Obs. Remote Sens.* 10, 4225–4236. <https://doi.org/10.1109/JSTARS.2017.2711482>.
- Madec, S., Baret, F., De Solan, B., Thomas, S., Dutartre, D., Jezequel, S., Hemmerle, M., Colombeau, G., Comar, A., 2017. High-throughput phenotyping of plant height: comparing unmanned aerial vehicles and ground LiDAR estimates. *Front. Plant Sci.* 8, 2002. <https://doi.org/10.3389/fpls.2017.02002>.
- Meng, Y., Song, J., Lan, Y., Mei, G., Liang, Z., Han, Y., 2019. Harvest aids efficacy applied by unmanned aerial vehicles on cotton crop. *Ind. Crops Prod.* 140, 111645 <https://doi.org/10.1016/j.indcrop.2019.111645>.
- Morsdorf, F., Nichol, C., Malthus, T., Woodhouse, I.H., 2009. Assessing forest structural and physiological information content of multi-spectral LiDAR waveforms by radiative transfer modelling. *Remote Sens. Environ.* 113, 2152–2163. <https://doi.org/10.1016/j.rse.2009.05.019>.
- Myinen, R., Williams, D., 1994. On the relationship between FAPAR and NDVI. *Remote Sens. Environ.* 49, 200–211. [https://doi.org/10.1016/0034-4257\(94\)90016-7](https://doi.org/10.1016/0034-4257(94)90016-7).
- N  asset, E., Bjerknes, K.-O., 2001. Estimating tree heights and number of stems in young forest stands using airborne laser scanner data. *Remote Sens. Environ.* 78, 328–340. [https://doi.org/10.1016/S0034-4257\(01\)00228-0](https://doi.org/10.1016/S0034-4257(01)00228-0).
- Nie, S., Wang, C., Dong, P., Xi, X., Luo, S., Zhou, H., 2016. Estimating leaf area index of maize using airborne discrete-return LiDAR data. *IEEE J. Sel. Top. Appl. Earth Obs. Remote Sens.* 9, 3259–3266. <https://doi.org/10.1109/JSTARS.2016.2554619>.
- Nurminen, K., Karjalainen, M., Yu, X., Hypp  , J., Honkavaara, E., 2013. Performance of dense digital surface models based on image matching in the estimation of plot-level forest variables. *ISPRS J. Photogramm. Remote Sens.* 83, 104–115. <https://doi.org/10.1016/j.isprsjrs.2013.06.005>.
- Omasa, K., Hosoi, F., Konishi, A., 2007. 3D lidar imaging for detecting and understanding plant responses and canopy structure. *J. Exp. Bot.* 58, 881–898. <https://doi.org/10.1093/jxb/erl142>.
- Parker, G.G., Russ, M.E., 2004. The canopy surface and stand development: assessing forest canopy structure and complexity with near-surface altimetry. *Ecol. Manag.* 189, 307–315. <https://doi.org/10.1016/j.foreco.2003.09.001>.
- Qi, J., Chehbouni, A., Huete, A.R., Kerr, Y.H., Sorooshian, S., 1994. A modified soil adjusted vegetation index. *Remote Sens. Environ.* 48, 119–126. [https://doi.org/10.1016/0034-4257\(94\)90134-1](https://doi.org/10.1016/0034-4257(94)90134-1).
- Ramoelo, A., Skidmore, A.K., Cho, M.A., Schlerf, M., Mathieu, R., Heitk  nig, I.M., 2012. Regional estimation of savanna grass nitrogen using the red-edge band of the spaceborne RapidEye sensor. *Int. J. Appl. Earth Obs. Geoinf.* 19, 151–162. <https://doi.org/10.1016/j.jag.2012.05.009>.
- Raper, T., Varco, J., 2015. Canopy-scale wavelength and vegetative index sensitivities to cotton growth parameters and nitrogen status. *Precis. Agric.* 16, 62–76. <https://doi.org/10.1007/s11119-014-9383-4>.
- Rondeaux, G., Steven, M., Baret, F., 1996. Optimization of soil-adjusted vegetation indices. *Remote Sens. Environ.* 55, 95–107. [https://doi.org/10.1016/0034-4257\(95\)00186-7](https://doi.org/10.1016/0034-4257(95)00186-7).
- Roujean, J.-L., Breon, F.-M., 1995. Estimating PAR absorbed by vegetation from bidirectional reflectance measurements. *Remote Sens. Environ.* 51, 375–384. [https://doi.org/10.1016/0034-4257\(94\)00114-3](https://doi.org/10.1016/0034-4257(94)00114-3).
- Ryu, Y., Nilson, T., Kobayashi, H., Sonnentag, O., Law, B.E., Baldocchi, D.D., 2010. On the correct estimation of effective leaf area index: Does it reveal information on clumping effects? *Agric. Meteorol.* 150, 463–472. <https://doi.org/10.1016/j.agrformet.2010.01.009>.
- Shao, M., Nie, C., Zhang, A., Shi, L., Zha, Y., Xu, H., Yang, H., Yu, X., Bai, Y., Liu, S., 2023. Quantifying effect of maize tassels on LAI estimation based on multispectral imagery and machine learning methods. *Comput. Electron. Agric.* 211, 108029 <https://doi.org/10.1016/j.compag.2023.108029>.
- Simonich, S.L., Hites, R.A., 1994. Importance of vegetation in removing polycyclic aromatic hydrocarbons from the atmosphere. *Nature* 370, 49–51. <https://doi.org/10.1038/370049a0>.
- Solberg, S., Brunner, A., Hanssen, K.H., Lange, H., N  asset, E., Rautiainen, M., Stenberg, P., 2009. Mapping LAI in a Norway spruce forest using airborne laser scanning. *Remote Sens. Environ.* 113, 2317–2327. <https://doi.org/10.1016/j.rse.2009.06.010>.
- Stanton, C., Starek, M.J., Elliott, N., Brewer, M., Maeda, M.M., Chu, T., 2017. Unmanned aircraft system-derived crop height and normalized difference vegetation index metrics for sorghum yield and aphid stress assessment. 026035–026035. *J. Appl. Remote Sens.* 11. <https://doi.org/10.1117/1.JRS.11.026035>.
- Tahir, M.N., Lan, Y., Zhang, Y., Wang, Y., Nawaz, F., Shah, M.A.A., Gulzar, A., Qureshi, W.S., Naqvi, S.M., Naqvi, S.Z.A., 2020. Real time estimation of leaf area index and groundnut yield using multispectral UAV. *Int. J. Precis. Agric. Aviat.* 3 <https://doi.org/10.33440/j.ijpaa.20200301.70>.
- Toth, C., J  zk  w, G., 2016. Remote sensing platforms and sensors: A survey. *ISPRS J. Photogramm. Remote Sens.* 115, 22–36. <https://doi.org/10.1016/j.isprsjrs.2015.10.004>.
- Tucker, C.J., 1979. Red and photographic infrared linear combinations for monitoring vegetation. *Remote Sens. Environ.* 8, 127–150. [https://doi.org/10.1016/0034-4257\(79\)90013-0](https://doi.org/10.1016/0034-4257(79)90013-0).
- Vi  a, A., Gitelson, A.A., Nguy-Robertson, A.L., Peng, Y., 2011. Comparison of different vegetation indices for the remote assessment of green leaf area index of crops. *Remote Sens. Environ.* 115, 3468–3478. <https://doi.org/10.1016/j.rse.2011.08.010>.
- Volpatto, L., Pinto, F., Gonz  lez-P  rez, L., Thompson, I.G., Bor  em, A., Reynolds, M., G  erard, B., Molero, G., Rodrigues Jr, F.A., 2021. High throughput field phenotyping for plant height using UAV-based RGB imagery in wheat breeding lines: feasibility and validation. *Front. Plant Sci.* 12, 591587 <https://doi.org/10.3389/fpls.2021.591587>.
- Xu, W., Chen, P., Zhan, Y., Chen, S., Zhang, L., Lan, Y., 2021. Cotton yield estimation model based on machine learning using time series UAV remote sensing data. *Int. J. Appl. Earth Obs. Geoinf.* 104, 102511 <https://doi.org/10.1016/j.jag.2021.102511>.
- Yang, H., Hu, X., Zhao, J., Hu, Y., 2021a. Feature extraction of cotton plant height based on DSM difference method. *Int. J. Precis. Agric. Aviat.* 4 <https://doi.org/10.33440/j.ijpaa.20210401.151>.
- Yang, X., Yang, R., Ye, Y., Yuan, Z., Wang, D., Hua, K., 2021b. Winter wheat SPAD estimation from UAV hyperspectral data using cluster-regression methods. *Int. J. Appl. Earth Obs. Geoinf.* 105, 102618 <https://doi.org/10.1016/j.jag.2021.102618>.
- Zhang, L., Sun, B., Zhao, D., Shan, C., Wang, G., Song, C., Chen, P., Lan, Y., 2024. Prediction of cotton FPAR and construction of defoliation spraying prescription map based on multi-source UAV images. *Comput. Electron. Agric.* 220, 108897 <https://doi.org/10.1016/j.compag.2024.108897>.
- Zhao, X., Guo, Q., Su, Y., Xue, B., 2016. Improved progressive TIN densification filtering algorithm for airborne LiDAR data in forested areas. *ISPRS J. Photogramm. Remote Sens.* 117, 79–91. <https://doi.org/10.1016/j.isprsjrs.2016.03.016>.
- Zhao, K., Suarez, J.C., Garcia, M., Hu, T., Wang, C., Londo, A., 2018. Utility of multitemporal lidar for forest and carbon monitoring: Tree growth, biomass dynamics, and carbon flux. *Remote Sens. Environ.* 204, 883–897. <https://doi.org/10.1016/j.rse.2017.09.007>.